

PAN-STARRS1 DISCOVERY OF TWO ULTRA-LUMINOUS SUPERNOVAE AT $z \approx 0.9$

L. CHOMIUK^{1,2}, R. CHORNOCK², A. M. SODERBERG², E. BERGER², M. E. HUBER³, G. NARAYAN⁴, A. REST⁵,
 R. A. CHEVALIER⁶, R. J. FOLEY², S. GEZARI³, R. P. KIRSHNER², A. RIESS³, S. A. RODNEY³, S. J. SMARTT⁷,
 C. W. STUBBS⁴, J. L. TONRY⁸, W. M. WOOD-VASEY⁹, W. S. BURGETT⁸, K. C. CHAMBERS⁸, H. FLEWELLING⁸,
 K. FORSTER¹⁰, N. KAISER⁸, R.-P. KUDRITZKI⁸, D. C. MARTIN¹⁰, J. S. MORGAN⁸, J. D. NEILL¹⁰, P. A. PRICE¹¹, AND
 R. J. WAINSCOT⁸

Submitted to the Astrophysical Journal

ABSTRACT

We present the discovery and analysis of two ultra-luminous supernovae (SNe) at $z \approx 0.9$ with the Pan-STARRS1 Medium-Deep Survey. These SNe, PS1-10ky and PS1-10awh, are amongst the most luminous SNe ever discovered, comparable to the unusual transient SCP 06F6. Like SCP 06F6, they show characteristic high luminosities ($M_{\text{bol}} \approx -22.5$ mag), blue spectra with a few broad absorption lines, and no evidence for H or He. We have constructed a full multi-color light curve sensitive to the peak of the spectral energy distribution in the rest-frame ultraviolet, and we have obtained time-series spectroscopy for these SNe. Given the similarities between the SNe, we combine their light curves to estimate a total radiated energy over the course of explosion of $(0.9 - 1.4) \times 10^{51}$ erg. We find expansion velocities of $12,000 - 18,000$ km s⁻¹ with no evidence for deceleration measured ~ 3 rest-frame weeks either side of light-curve peak, consistent with the expansion of an optically-thick massive shell of material. We show that radioactive decay is not sufficient to power PS1-10ky, and discuss two plausible origins for these events: the initial spin-down of a newborn magnetar in a core-collapse SN, or SN shock breakout from the dense circumstellar wind surrounding a Wolf-Rayet star.

Subject headings: supernovae: general, supernovae: individual (PS1-10ky, PS1-10awh, SCP 06F6), circumstellar matter, Stars: magnetars

1. INTRODUCTION

The observational and physical parameter space occupied by supernovae (SNe) has expanded dramatically because of the recent discovery of several ultra-luminous SNe. These SNe are significantly more luminous than Type Ia explosions, displaying absolute bolometric magnitudes at light curve maximum of < -21 mag and total radiated energies on the order of 10^{51} erg. Thus far, ultra-luminous SNe have displayed impressive diversity, ranging from the Type Ic SN 2007bi, proposed to be a pair-instability explosion (Gal-Yam et al. 2009; Young et al. 2010), to the Type IIn SN 2006gy, with strong signs of circumstellar interaction (Smith et al. 2007; Smith & McCray 2007;

Ofek et al. 2007). The mysterious transient SCP 06F6 discovered by Barbary et al. (2009) showed a largely featureless spectrum with a few broad absorption lines, and proved so perplexing that no redshift could be identified. Because it was uncertain if the source was Galactic or at a cosmological distance, many ideas were presented to explain it ranging from an outburst on a white dwarf to a broad-lined QSO (Barbary et al. 2009; Gänsicke et al. 2009; Chatzopoulos et al. 2009; Soker et al. 2010).

Since SCP 06F6 was discovered by Barbary et al. (2009), similar objects have been found with significant frequency in wide-field transient surveys. Quimby et al. (2011) collected five additional SCP 06F6-like sources discovered by the Texas Supernova Survey and the Palomar Transient Factory (PTF), including the earlier-identified SN 2005ap (Quimby et al. 2007). They identified narrow Mg II $\lambda\lambda 2796, 2803$ absorption lines in their spectra, presumably associated with the interstellar media of the host galaxies. From this absorption, they derived redshifts ranging from $0.25 \lesssim z \lesssim 0.5$ for their sources, and a redshift of $z = 1.19$ for SCP 06F6 itself. These cosmological distances imply that the SCP 06F6-like sources are some of the most luminous SNe known, with peak absolute magnitudes $M_U \lesssim -22$ mag and total radiated energies $\gtrsim 10^{51}$ erg.

With their redshifts known, a common set of observational properties began to emerge for the SCP 06F6-like objects. In addition to their very high peak luminosities, these sources all show distinctive symmetric light curves with rise and decline times on the order of 30 days in the rest frame. They also all show blue spectra with only a handful of features; Quimby et al. (2011) identify the broad absorption lines with light metals (C, O, Si, and

lchomiuk@cfa.harvard.edu

¹ National Radio Astronomy Observatory, P.O. Box O, Socorro, NM 87801 USA

² Harvard-Smithsonian Center for Astrophysics, 60 Garden Street, Cambridge, MA 02138, USA

³ Department of Physics and Astronomy, Johns Hopkins University, 3400 North Charles Street, Baltimore, MD 21218, USA

⁴ Department of Physics, Harvard University, Cambridge, MA 02138, USA

⁵ Space Telescope Science Institute, 3700 San Martin Drive, Baltimore, MD 21218, USA

⁶ Department of Astronomy, University of Virginia, P.O. Box 400325, Charlottesville, VA 22904-4325

⁷ Astrophysics Research Centre, School of Mathematics and Physics, Queen's University Belfast, Belfast, BT7 1NN, UK

⁸ Institute for Astronomy, University of Hawaii at Manoa, Honolulu, HI 96822, USA

⁹ Department of Physics and Astronomy, University of Pittsburgh, 3941 O'Hara Street, Pittsburgh, PA 15260, USA

¹⁰ California Institute of Technology, 1200 E. California Blvd., Pasadena, CA 91125, USA

¹¹ Department of Astrophysical Sciences, Princeton University, Princeton, NJ 08544, USA

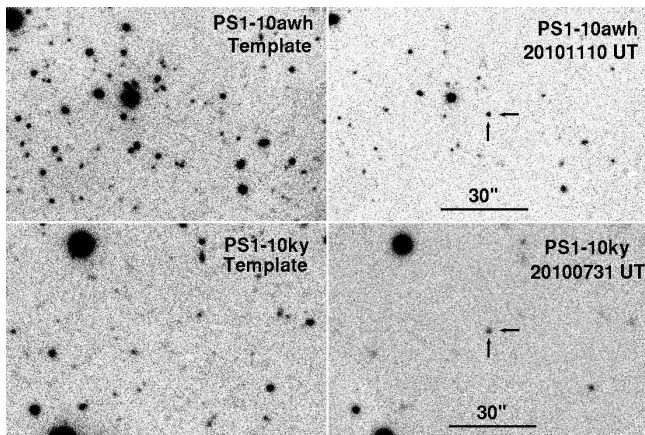


FIG. 1.— Cut-outs of PS1 i_{P1} -band images showing the region around PS1-10awh (top) and PS1-10ky (bottom). The left column shows stacked images using data before explosion; the right column shows images from single nights around maximum light.

Mg). There is no clear evidence for H or He in the spectra of an SCP 06F6-like transient, although Quimby et al. (2007) note a broad feature in SN 2005ap that may be associated with $H\alpha$. There also is no detection of strong Fe II or Fe III lines in the early or peak spectra of these transients.

Subsequently, the ultra-luminous SN 2010gx was discovered by both the Catalina Real-time Transient Survey (Mahabal et al. 2010; Mahabal & Drake 2010) and PTF (Quimby et al. 2010), and was determined to be at $z = 0.23$. Pastorello et al. (2010) carried out a detailed study of this source, which shows SCP 06F6-like spectral features and high luminosity at early times. They find that, a few weeks after peak light, this source begins to show iron and other features indicative of Type Ic SNe. They assert that SCP 06F6-like objects are likely to be associated with SNe Ibc, consistent with the lack of H in their spectra.

Two potential explanations for these SCP 06F6-like sources have surfaced: the interaction of the SN shock with a dense circumstellar shell of H-poor material (e.g., Chevalier & Irwin 2011) or the spin-down of a new-born magnetar embedded in the SN ejecta (Kasen & Bildsten 2010; Woosley 2010). Both of these models have the potential to explain the high luminosities and association with SNe Ibc.

Here, we present two new ultra-luminous SNe at $z \approx 0.9$ discovered with Panoramic Survey Telescope & Rapid Response System 1 (Pan-STARRS1, abbreviated as PS1 here). By combining data for these two sources, we obtain the first full composite multi-color light curve for SCP 06F6-like objects and place constraints on the origins of these sources. Our photometry in multiple filters allows us to measure the color evolution of these sources, while their high redshifts aid in measuring bolometric luminosities, as these sources' spectral energy distributions (SEDs) peak in the rest-frame ultraviolet. Our spectroscopic observations sample the entire light curve, enabling us to measure the evolution of photospheric velocities. These measurements place important constraints on any model that attempts to explain these sources' high luminosities.

In §2, we describe our data, obtained using PS1, MMT, Gemini, *GALEX*, and the EVLA. In §3 we constrain

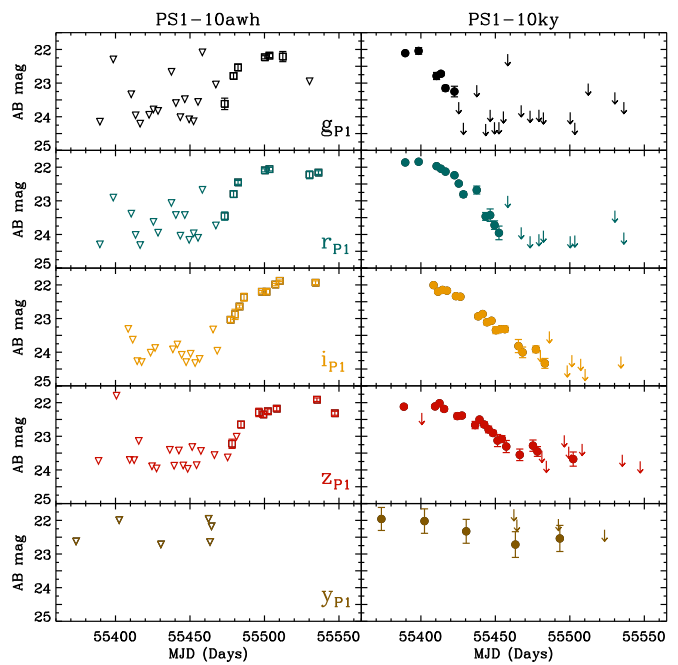


FIG. 2.— Observed light curves for PS1-10awh (left column) and PS1-10ky (right column) in five filters from top to bottom: g_{P1} (black), r_{P1} (blue), i_{P1} (gold), z_{P1} (red), and y_{P1} (brown). Apparent AB magnitudes are plotted as a function of modified Julian day, with squares and circles representing PS1-10awh and PS1-10ky respectively, and 3σ upper limits denoted by triangles and arrows.

the properties of the host galaxies. In §4, 5, and 6, we measure the evolution of their photospheric temperatures, bolometric luminosities, and photospheric velocities, combining our new data with published data of SCP 06F6 and SN 2010gx. In §7, we consider three possible physical scenarios that might explain the characteristics of these sources: radioactive decay, magnetar spin-down, and circumstellar interaction. Finally in §8, we summarize our results.

2. OBSERVATIONS

2.1. PS1 Photometry

2.1.1. PS1 Survey Summary

The PS1 system is a high-etendue wide-field imaging system, designed for dedicated survey observations. The system is installed on the peak of Haleakala on the island of Maui in the Hawaiian island chain. Routine observations are conducted remotely, from the Waiakoa Laboratory in Pukalani. A complete description of the PS1 system, both hardware and software, is provided by Kaiser et al. (2010). The survey design and execution strategy are described in K. C. Chambers et al. (2011, in preparation).

The PS1 optical design (Hodapp et al. 2004) uses a 1.8 meter diameter $f/4.4$ primary mirror, and a 0.9 m secondary. The resulting converging beam then passes through two refractive correctors, a $48 \text{ cm} \times 48 \text{ cm}$ interference filter, and a final refractive corrector that is the dewar window. The telescope delivers an image with a diameter of 3.3 degrees, with low distortion. The PS1 imager (Tonry & Onaka 2009) comprises a total of 60 4800×4800 pixel detectors, with $10 \mu\text{m}$ pixels that subtend 0.258 arcsec, providing an instantaneous field of

view of 7.1 sq. deg. The detectors are back-illuminated CCDs manufactured by Lincoln Laboratory. The detectors are read out using a StarGrasp CCD controller, with a readout time of 7 seconds for a full unbinned image. Initial performance assessments are presented in Onaka et al. (2008).

The PS1 observations are obtained through a set of five broadband filters, which we have designated as g_{P1} , r_{P1} , i_{P1} , z_{P1} , and y_{P1} . Although the filter system for PS1 has much in common with that used in previous surveys, such as Sloan Digital Sky Survey (SDSS; York et al. 2000; Abazajian et al. 2009), there are important differences. The g_{P1} filter extends 200 Å redward of g_{SDSS} , paying the price of 5577 Å sky emission for greater sensitivity and lower systematics for photometric redshifts, and the z_{P1} filter is cut off at 8400 Å, giving it a different response than the detector response defined z_{SDSS} . SDSS has no corresponding y_{P1} filter. Further information on the passband shapes is described in Stubbs et al. (2010). Provisional response functions (including 1.3 airmasses of atmosphere) are available at the project’s web site¹. Photometry is in the “natural” PS1 system, $m = -2.5 \log(\text{flux}) + m'$, with a single zeropoint adjustment m' made in each band to conform to the AB magnitude scale. Zeropoints were measured from comparison with field stars in the SDSS catalog, but no color corrections were made to determine the magnitudes exactly in the SDSS system.

The PS1 Medium Deep Survey (MDS) accounts for approximately 25% of observing time. It revisits ten fields (each equivalent to a single PS1 imager footprint) on a nearly nightly basis in g_{P1} , r_{P1} , i_{P1} , z_{P1} , and y_{P1} bands (Stubbs et al. 2010), reaching a typical 3σ limiting magnitude of ~ 23.5 mag in one visit at g_{P1} , r_{P1} , i_{P1} , and z_{P1} bands and ~ 21.7 mag in y_{P1} . The MDS fields are distributed across the sky, so only a subset of fields are observed at any given time of year, and on any given night only in a subset of bands, depending on observing conditions.

The MDS images are processed through the Image Processing Pipeline (IPP; Magnier 2006), on a computer cluster at the Maui High Performance Computer Center. The pipeline runs the images through a succession of stages, including flat-fielding (“de-trending”), a flux-conserving warping to a sky-based image plane, masking and artifact removal, and object detection and photometry. Difference images are produced from the stacked images by the **photpipe** pipeline (Rest et al. 2005) and potential transients are visually inspected by humans for possible promotion to the status of transient alerts. The IPP-photpipe system finds hundreds of transient alerts per month, of which a subset are targeted for spectroscopic confirmation.

2.1.2. PS1-10ky and PS1-10awh

PS1-10awh and PS1-10ky were discovered by the PS1 MDS at J2000 locations of R.A. = $22^{\text{h}}14^{\text{m}}29^{\text{s}}.831$, Dec = $-00^{\circ}04'03''.62$ and R.A. = $22^{\text{h}}13^{\text{m}}37^{\text{s}}.851$, Dec = $+01^{\circ}14'23''.57$, respectively (uncertainty in positions ≈ 0.05 arcsec). PS1-10ky was apparent immediately when

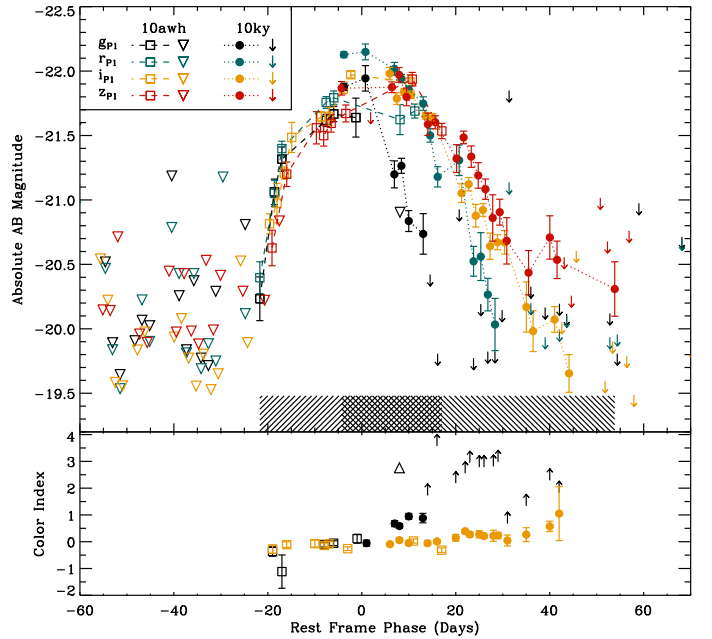


FIG. 3.— Top Panel: Combined light curve for PS1-10awh and PS1-10ky in four filters that have been red-shifted to the central wavelengths listed in Table 1: g_{P1} (black), r_{P1} (blue), i_{P1} (gold), and z_{P1} (red). Measurements for PS1-10awh are marked as open squares connected with dashed lines; 3σ upper limits are denoted by open triangles. For PS1-10ky, measurements are shown as filled circles connected with dotted lines, and upper limits are signified with arrows. Rest frame times and absolute magnitudes are calculated using measured redshifts of $z = 0.908$ and $z = 0.956$, respectively. To highlight the overlap of the two light curves, the time ranges during which each SN is detected in PS1 photometry are marked as hatched regions at the bottom of the plot. Bottom Panel: The time evolution of $g_{P1} - z_{P1}$ color in black and $i_{P1} - z_{P1}$ color in gold. Measurements and limits for PS1-10awh are marked as squares and triangle respectively, while measurements and limits for PS1-10ky are shown as circles and arrows.

observations began of the MD09 field in June 2010. It was discovered near peak brightness and had faded below PS1 MDS sensitivity by November 2010. PS1-10awh was first detected in early October 2010 by its rising flux, and was observed almost every night by PS1 MDS until Field MD09 set in early December. Figure 1 shows the vicinities of the SNe before explosion and around maximum light. Both objects were selected for spectroscopic followup at the MMT and Gemini based on the lack of visible host galaxies in the template images and were then confirmed as high-redshift supernovae.

Photpipe measures SN photometry using forced-centroid PSF-fitting photometry on the difference images, with a PSF appropriate to each difference image, and a common centroid derived from the high SNR detections. The measured AB magnitudes for PS1-10awh and PS1-10ky are listed in Tables 4 and 5 and plotted in Figure 2, along with 3σ upper limits for epochs with non-detections. We corrected for foreground extinction using Schlegel et al. (1998) values and the Cardelli et al. (1989) extinction law, but did not correct for any intrinsic extinction.

To calculate absolute magnitudes, we did not carry out a full k -correction, but instead only corrected the measured magnitudes for cosmological expansion using

¹ http://svn.pan-starrs.ifa.hawaii.edu/trac/ipp/wiki/PS1_Photometric_System

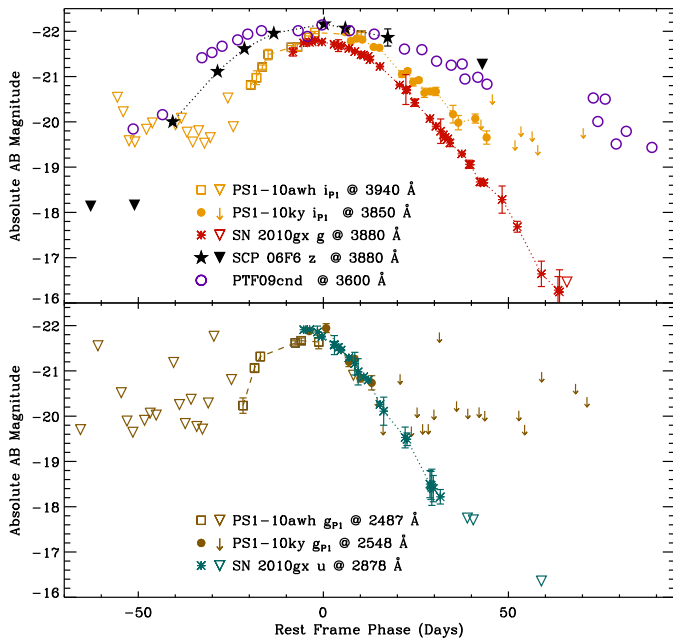


FIG. 4.— A comparison of light curves for SCP 06F6-like ultra-luminous SNe. In the top panel, we compare i_{P1} band light curves for PS1-10awh and PS1-10ky with SN 2010gx g band measurements and SCP 06F6 z band measurements, all of which fall at comparable rest wavelengths around 3900 Å. Similarly in the bottom panel, we compare the g_{P1} band measurements of PS1-10awh and PS1-10ky with the u band light curve of SN 2010gx, to probe blue wavelengths around ~ 2600 Å (no bluer photometry is available for SCP 06F6).

the redshifts measured from Mg II absorption (§2.2):

$$M = m - 5 \log \left(\frac{d_L}{10 \text{ pc}} \right) + 2.5 \log (1 + z) \quad (1)$$

where m is the apparent magnitude, d_L is the luminosity distance, and M is the corresponding absolute magnitude. We did not shift the central wavelengths at which flux densities were measured (see Table 1 for central wavelengths in the rest frame, which are weighted by the system response). The similar redshifts of PS1-10ky ($z = 0.956$) and PS1-10awh ($z = 0.908$) ensure that the rest wavelengths and passbands of the photometry will be comparable.

The light curves show similar peak luminosities, widths, and color evolution. We find that we can splice them together to produce a full light curve if we set the peak date to 2010 July 20 for PS1-10ky and to 2010 November 20 for PS1-10awh (Figure 3). For both objects, we observe the peak of the light curve, implying that PS1-10awh fully represents the light curve rise and PS1-10ky samples the light curve decline. Uncertainties in the splicing (or in our implicit assumption that these two sources are very similar) will only affect *comparisons* of the rise and the decline. We have overlapping light curve coverage for ~ 18 rest-frame days around peak (see hatched region in Figure 3). The splicing of the light curves is well-constrained by a few late-time measurements of PS1-10awh: notably the z_{P1} measurement from 2010 December 10 and the g_{P1} upper limit from 2010 December 5, which both show a declining light curve (Figure 2). Note the well-matched rapid fall off in

TABLE 1
CENTRAL REST WAVELENGTHS OF OPTICAL PASSBANDS (Å)

Filter ^a	PS1-10awh	PS1-10ky	SN 2010gx	SCP 06F6
u	—	—	2878	—
g	2550	2488	3878	—
r	3267	3188	5065	—
i	3944	3848	6199	3540
z	4536	4426	7426	3883
y	5097	4974	—	—

^a These are PS1 filters (Stubbs et al. 2010) for PS1-10ky and PS1-10awh, SDSS filters for SN 2010gx, and *Hubble Space Telescope*/ACS filters *F775W* and *F850LP* for SCP 06F6.

the g_{P1} band for both sources (Figure 3), implying that they have a similar color evolution.

In Figure 4, we compare the combined light curve from PS1-10ky and PS1-10awh with the ultra-luminous transient SCP 06F6 (Barbary et al. 2009; Quimby et al. 2011; $z = 1.19$) and SN 2010gx (Pastorello et al. 2010; $z = 0.23$). The combination of our two PS1 SNe show a light curve that falls off much more slowly at the redder (~ 3900 Å; gold points) bands, as compared with the bluer (~ 2500 Å; black points) measurements. SN 2010gx was not well observed on the rise, although the one meaningful upper limit (unfiltered; Pastorello et al. 2010) is suggestive of a faster rise to maximum than the other three. Its decline shows the bluer filter declining much faster than the redder, in good accord with PS1-10ky and PS1-10awh. The sources' peak luminosities agree to within $\sim 25\%$ and the widths of the light curves are similar. From the commonalities in their light curves, along with the similarities in their spectra (§2.2), we conclude that these four sources all belong to the common class of SCP 06F6-like ultra-luminous SNe pointed out by Quimby et al. (2011).

2.2. Spectroscopy

We obtained four optical spectra of PS1-10ky and three spectra of PS1-10awh using MMT (Hectospec and Blue Channel Spectrographs) and Gemini (GMOS; Table 2). Basic spectroscopic processing and extraction were accomplished using standard routines in IRAF, or using the OIR Telescope Data Center pipeline in the case of MMT/Hectospec data (Mink et al. 2007). We then used custom IDL routines to apply flux calibrations and remove telluric absorption based on observations of spectrophotometric standard stars. Narrow Mg II $\lambda\lambda 2796, 2803$ absorption, arising from the interstellar medium of the SN host galaxy, is seen in all spectra with wavelength coverage of the doublet (Figure 5). From this absorption, we measure a redshift of $z = 0.9084$ for PS1-10awh and $z = 0.9558$ for PS1-10ky. These correspond to luminosity distances of $d_L = 5890$ Mpc and $d_L = 6270$ Mpc for a cosmology with $H_0 = 71 \text{ km s}^{-1} \text{ Mpc}^{-1}$, $\Omega_M = 0.27$, and $\Omega_\Lambda = 0.73$.

The spectra are shown in Figure 6, along with the SCP 06F6 spectra from Barbary et al. (2009) and spectra of SN 2010gx from Pastorello et al. (2010). As with the photometry, we corrected them for foreground extinction (Schlegel et al. 1998; Cardelli et al. 1989). In many cases, clouds were present during observations so the absolute flux scaling of the spectra can not be trusted, but

TABLE 2
SPECTROSCOPIC OBSERVATIONS

Date	Phase ^a (Days)	Facility	Grating/ Central λ (Å)	λ Range ^b (Å)	Res ^c (Å)	Airmass	Slit P.A. (deg)
PS1-10ky:							
2010 Jul 17	−2	MMT/Blue Channel ^d	300/6006	3393–8623	5.5	1.2	326
2010 Jul 21	1	Gemini-N/GMOS ^e	B600/4800	3390–6220	4.7	1.1	180
2010 Aug 18	15	Gemini-S/GMOS	B600/5000	3600–6432	4.7	1.3	180
2010 Sep 09	26	Gemini-S/GMOS	R400/8000	5887–10161	8.0	1.4	180
PS1-10awh:							
2010 Oct 12	−21	Gemini-N/GMOS	R400/7500	5441–9655	5.0	1.3	210
2010 Nov 27	4	MMT/Hectospec ^f	270/6500	3700–9150	4.9	1.2	Fiber
2010 Dec 09	10	MMT/Blue Channel	300/5768	3230–8325	5.5	1.5	40

^a In the rest frame.

^b In the observer frame.

^c Approximate spectral resolution, measured from widths of night sky lines.

^d Schmidt et al. (1989). ^eHook et al. (2004). ^fFabricant et al. (2005).

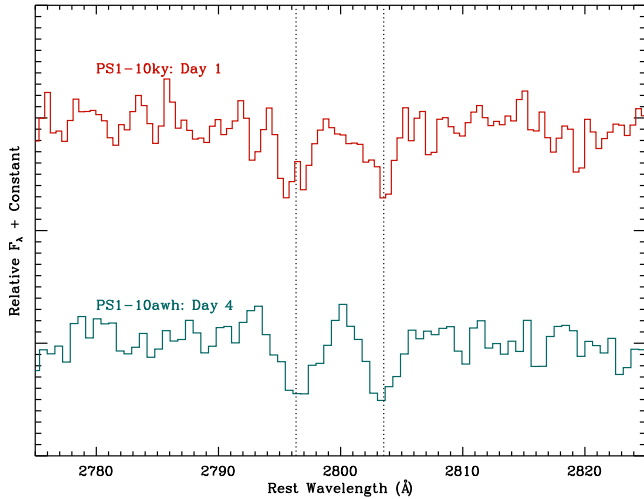


FIG. 5.— Detail of two spectra with wavelength coverage of the Mg II $\lambda\lambda 2796, 2803$ doublet, redshifted to $z = 0.9084$ for PS1-10awh and $z = 0.9558$ for PS1-10ky. The rest wavelengths of the Mg II doublet are shown as vertical dotted lines.

the general shape of the continuum is reliable.

The three broad absorption features between 2000 and 2900 Å were identified by Quimby et al. (2011) as C II (~ 2330 Å), Si III (2543 Å), and Mg II (2800 Å). The broad “W”-shaped features around 4300 Å, identified by Quimby et al. (2011) as O II, can be seen in the GMOS spectrum of PS1-10awh observed on Day −21.

Note that PS1-10ky and PS1-10awh show spectral features that become weaker as time progresses; our later spectra on PS1-10ky appear almost featureless. In SN 2010gx, the 4300 Å “W” feature has disappeared and the spectrum is practically featureless by Day 4, but then subsequently it shows strong SN Ic-like features of Fe II, Ca II, and Mg II. We are not very sensitive to similar features in PS1-10ky and PS1-10awh because of our blue rest-frame wavelength coverage (Figure 6). Our last spectrum, observed with relatively red wavelength coverage, was observed 26 days after peak and is rather noisy, but may show low signal-to-noise ratio depressions around rest wavelengths of 4350 Å and 4900 Å which might be consistent with the Fe II and Mg II features in

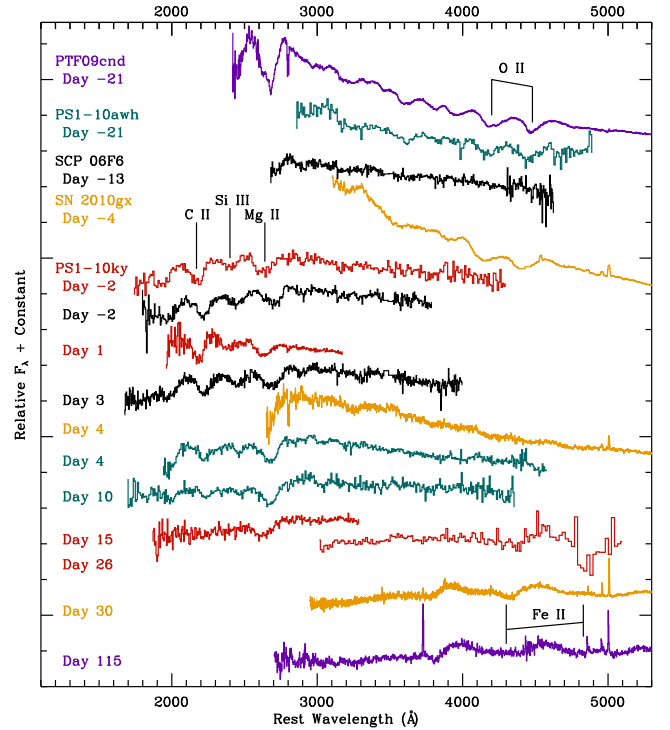


FIG. 6.— Spectra of PS1-10awh in blue, PS1-10ky in red, SN 2010gx (from Pastorello et al. 2010) in gold, and SCP 06F6 (from Barbary et al. 2009) in black. The time of each spectrum, relative to light curve peak in the rest frame, is marked on the left. Also marked are strong spectral features, tentatively identified as C II, O II, Si III, Mg II, and Fe II as discussed in the text.

SN 2010gx.

It is remarkable that no lines of H or He have ever been detected from an SCP 06F6-like object, although we note that none of the spectra in Figure 6 cover H α and the few that provide coverage of H β are very noisy. Similarly with He, the strongest lines are redward of 5000 Å and outside our spectroscopic coverage. However, the spectra obtained on low-redshift SCP 06F6-like objects by Quimby et al. (2011) and Pastorello et al. (2010) do cover this red portion of the spectrum, and no trace of H or He has been detected in these studies. In the future, deep infrared spectroscopy will be critical for plac-

ing strong limits on the presence of H or He.

2.3. GALEX Photometry

MD09 was observed with *GALEX* in August–September 2010. Both PS1-10ky and PS1-10awh—and their hosts—were non-detections in the NUV band. PS1-10ky was observed by *GALEX* near optical peak brightness, but PS1-10awh was observed before its rise. NUV 3σ upper limits are listed in Tables 4 and 5. The upper limits of $\gtrsim 23.5$ mag (AB system) correspond to a luminosity limit of $\lesssim 1.0 \times 10^{41}$ erg s $^{-1}$ Å $^{-1}$ at a central rest wavelength of 1161 Å for PS1-10ky.

2.4. EVLA Radio Continuum Measurements

We observed both ultra-luminous SNe with the EVLA as part of our NRAO Key Science Project “Exotic Explosions, Eruptions, and Disruptions: A New Transient Phase-Space”. We observed at 4.9 GHz with 256 MHz of bandwidth; time on source was 37 minutes for both sources. Gains were calibrated using J2212+0152, and the absolute flux density scale was calibrated using 3C48. PS1-10awh was observed on 2010 Dec 12, approximately three weeks after optical peak (observer frame), and yielded a non-detection of -22 ± 15 μ Jy beam $^{-1}$. PS1-10ky was observed on 2011 Feb 12, almost seven months after peak; we measured a non-detection of -2 ± 17 μ Jy beam $^{-1}$ at its location.

The gamma-ray burst (GRB) 030329 would have had a peak 4.9 GHz flux density of ~ 200 μ Jy at the distance of our ultra-luminous SNe, and would have remained a $> 3\sigma$ source for ~ 100 days (van der Horst et al. 2005; Frail et al. 2005). On the other hand, a weak GRB like 980425 and its associated SN 1998bw would be significantly below our detection limit, with a 4.8 GHz peak flux density of 2 μ Jy at a distance of 6000 Mpc (Kulkarni et al. 1998). It is unlikely, although not impossible given the spread in GRB radio luminosities (Soderberg 2007), that either PS1-10awh or PS1-10ky hosted a GRB.

3. HOST GALAXIES

We stacked the pre-explosion images of PS1-10awh (prior to 2010 Sept 21) to derive upper limits on the host galaxy’s luminosity. We find 3σ upper limits on apparent magnitude of $g_{P1} > 26.6$, $r_{P1} > 26.6$, $i_{P1} > 26.7$, $z_{P1} > 26.3$, and $y_{P1} > 24.2$ mag. Our z_{P1} -band limit roughly corresponds to $M_B > -17.0$ mag or $< 0.02 L^*$ (assuming $M_B^* = -21.3$ mag at a redshift of 0.9; Faber et al. 2007). Similarly, we stacked the 2009 data for PS1-10ky and found apparent magnitude limits of $g_{P1} > 26.1$, $r_{P1} > 26.0$, $i_{P1} > 25.9$, $z_{P1} > 25.3$, and $y_{P1} > 23.3$ mag. The z_{P1} -band limit translates to $M_B > -18.0$ mag or $< 0.05 L^*$.

The g_{P1} band is centered at ~ 2500 Å, in the NUV spectral range commonly used as a tracer of the photospheres of young massive stars, and thereby star formation rate (SFR). Using the calibration of Kennicutt (1998) and assuming no dust extinction, our limits on the g_{P1} -band host galaxy luminosities translate to SFR $< 0.4 M_\odot \text{ yr}^{-1}$ for PS1-10ky and $< 0.3 M_\odot \text{ yr}^{-1}$ for PS1-10awh. We also stacked the three spectra for PS1-10awh and detected [O II] $\lambda 3727$ emission at a luminosity of $4.5 \pm 1.0 \times 10^{40}$ erg s $^{-1}$. This translates to a SFR of

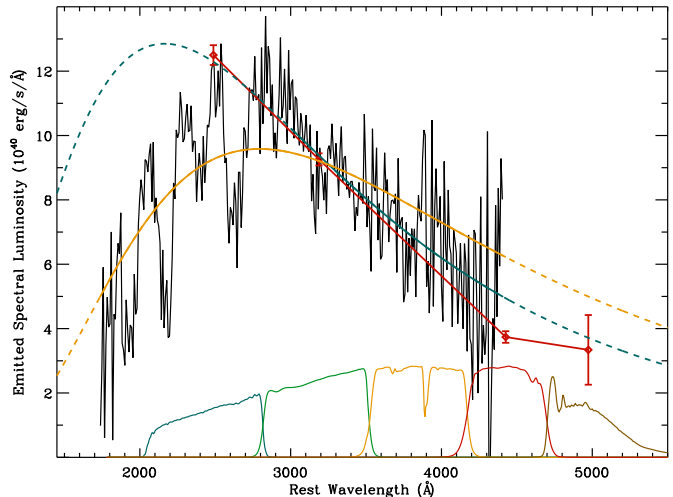


FIG. 7.— Spectrum of PS1-10ky observed at a phase of -2 days. Our PS1 photometry is overlain as red points connected with lines; the system response functions of the g_{P1} , r_{P1} , i_{P1} , z_{P1} , and y_{P1} filters are also shown at the bottom of the plot for reference. A blackbody fit to the full spectrum ($T = 10,000$ K) is shown as a solid gold line, and its extension to other wavelengths is represented by the gold dashed line. Similarly, the blackbody fit to the spectrum redward of 3000 Å ($T = 13,000$ K) is shown as a blue line.

$0.4 \pm 0.2 M_\odot \text{ yr}^{-1}$ (Kewley et al. 2004), consistent with the NUV limits given the significant uncertainties and our poor understanding of dust extinction in these systems. We did not stack the PS1-10ky spectra, as the redshift of this source places the [O II] emission line on a telluric feature.

These constraints are consistent with the host galaxies of other ultra-luminous SNe (Neill et al. 2011), which typically have low masses (less than the Large Magellanic Cloud), relatively low SFRs (70% of the Neill et al. sample has SFR $< 1 M_\odot \text{ yr}^{-1}$), and high specific SFRs. This preference for low-mass hosts is reminiscent of GRBs, which also display a bias towards lower-mass hosts with high specific SFR (e.g., Le Floc’h et al. 2003; Christensen et al. 2004). In the context of GRBs, this bias is often attributed to a collapsar origin (MacFadyen & Woosley 1999). The mass–metallicity relationship for galaxies (Tremonti et al. 2004) implies that lower-mass galaxies will be more metal poor, and metal-poor SN progenitors will undergo less wind-driven mass loss and maintain more angular momentum. However, a recent alternative hypothesis has been offered in which, because low-mass galaxies have higher specific SFRs, the observed bias of GRBs towards low-mass hosts is in fact simply a demonstration that they are associated with young stellar populations (Kocevski & West 2011; Mannucci et al. 2011).

4. COLOR EVOLUTION

In order to understand the basic physical parameters of these ultra-luminous SNe, we need to constrain their temperature evolution. The SEDs of SCP 06F6-like objects can be reasonably fit as blackbodies at redder wavelengths, but appear to suffer severe line blanketing blueward of 3000 Å. This was pointed out for SN 2010gx by Pastorello et al. (2010) and is apparent in Figure 7, where we show a spectrum of PS1-10ky with a blackbody

TABLE 3
SPECTROSCOPIC MEASUREMENTS

Date	Phase ^a (Days)	Temperature (K)	Velocity ^b (10^3 km s^{-1})	FWHM ^c (10^3 km s^{-1})
<u>PS1-10ky:</u>				
2010 Jul 17	−2	13,400±2700	19	12
2010 Jul 21	1	18,400±9000	20	13
2010 Aug 18	15	9600±4800	19	14
2010 Sep 09	26	7400±1100	—	—
<u>PS1-10awh:</u>				
2010 Oct 12	−21	18,100±3600	15 ^d	11 ^d
2010 Nov 27	4	19,700±3900	11	9
2010 Dec 09	10	10,200±2000	11	9
<u>SCP 06F6:^e</u>				
2006 Apr 22	−13	19,800±4000	—	—
2006 May 18	−2	13,000±2600	12	12
2006 May 28	3	13,600±1400	13	12
<u>SN 2010gx:^f</u>				
2010 Mar 21	−5	16,300±1600	19 ^d	12 ^d
2010 Mar 22	−4	15,200±800	19 ^d	9 ^d
2010 Apr 01	4	15,000±2300	—	—
2010 Apr 09	10	12,900±1900	19 ^g	12 ^g
2010 Apr 22	21	10,400±1600	17 ^g	16 ^g
2010 May 02	30	6900±1000	15 ^g	9 ^g
2010 Jun 05	57	5100±500	—	—

^a In the rest frame.

^b Velocity corresponding to line center for the three features in the blue (rest wavelengths of ~ 2330 , 2540 , and 2800 \AA) unless otherwise noted. Typical errors of $\sim 1000 \text{ km s}^{-1}$.

^c Average FWHM for the three features in the blue, unless otherwise noted. Typical errors of $\sim 3000 \text{ km s}^{-1}$.

^d This is a red spectrum, so velocities were measured from the O II “W” feature at $\sim 4300 \text{ \AA}$.

^e Spectra from Barbary et al. (2009).

^f Spectra from Pastorello et al. (2010).

^g Measured using the broad Fe II+Mg II feature around 4300 \AA .

fit to the full spectrum ($T = 10,400 \text{ K}$) and a fit to the spectrum redward of 3000 \AA ($T = 13,400 \text{ K}$). Clearly, no good blackbody fit is achievable when the bluest wavelengths are included, and the luminosity at $\lesssim 2500 \text{ \AA}$ is significantly damped from what is expected for the blackbody fit to the redder wavelengths. All of the spectra in Figure 6 turn over blueward of 3000 \AA , so we fit blackbodies to our data redward of 3000 \AA .

We carried out least-squares fits of Planck functions to the spectra shown in Figure 6; the best-fit temperatures and errors are listed in Table 3. We also fit color temperatures to the photometric data points for PS1-10awh, PS1-10ky, and SN 2010gx by interpolating the measured fluxes in time with a cubic spline and then least-squares fitting a blackbody spectrum on each rest-frame day which is constrained by measurements at three or more bands with central wavelengths redward of 3000 \AA . An interpolated flux on a given day is considered “constrained” if there is a $>3\sigma$ measurement both preceding it and following it in time. At times when there are only two bands with constrained flux measurements redward of 3000 \AA , we fit the colors by calculating a grid of predicted colors for various blackbody temperatures (grid resolution of 250 K) and identifying the closest blackbody temperature to the measured color. Errors in color are directly translated to errors in temperature by us-

ing this grid in a similar fashion. Temperature fits are shown in the top panel of Figure 8. Jumps in temperature or in the size of the error bars (e.g., around Day -7 for PS1-10awh) are caused by transitions from least-squares fitting to color fitting; single color fits have much larger error bars and in some temperature regimes, they show systematic bias. This is likely due to features in the spectra which can cause significant deviations from a blackbody spectrum over several hundred angstroms (Figure 6).

The spectroscopic and photometric temperature measurements agree rather well, and the color temperatures of all four ultra-luminous SNe are consistent with one another. The temperature evolution is modeled with a quadratic fit to the combined measurements for all four SNe (solid black line in Figure 8) showing a maximum temperature of $\sim 24,000 \text{ K}$ at early times (with significant uncertainty) and a minimum temperature of $\sim 5000 \text{ K}$ at late times.

From Figure 7, we see that even in the absence of line blanketing, we would not expect GALEX detections with $< 23.5 \text{ mag}$ (corresponding to $\lesssim 1.0 \times 10^{41} \text{ erg s}^{-1} \text{ \AA}^{-1}$ at 1161 \AA). The first GALEX observation of PS1-10ky occurred at ~ 6 days after maximum, when the temperature was cooler and the ultraviolet luminosity would have been even fainter than that predicted in Figure 7.

We note that the C II and Si III absorption have largely

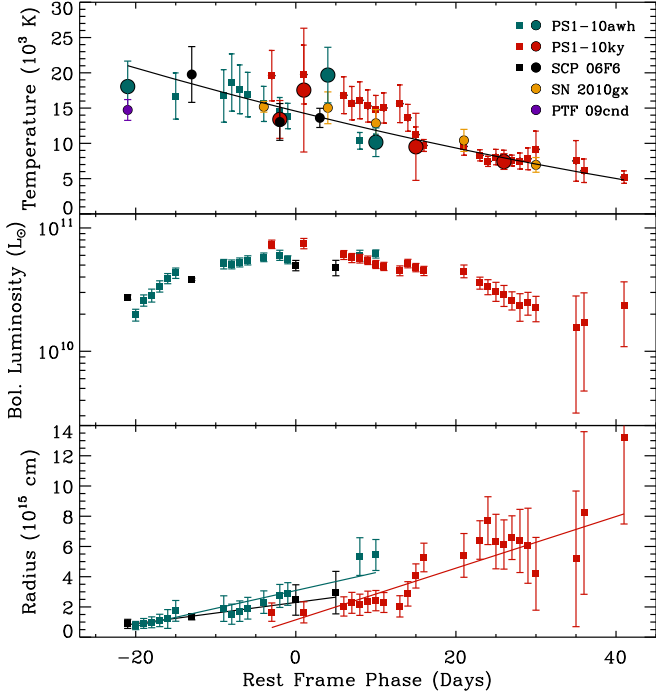


FIG. 8.— Top Panel: Temperature as a function of rest-frame time. Squares denote measurements from photometry, while circles are spectroscopic measurements. The quadratic fit to these data is marked as a black solid line. Middle Panel: Bolometric luminosity as a function of time. These are determined by summing up flux in the measured photometric bands and extrapolating a blackbody tail to the red; emission blueward of 2100 Å for PS1-10ky/PS1-10awh, 2600 Å for SN 2010gx, and 3150 Å for SCP 06F6 is not accounted for, implying that these are lower limits. Bottom Panel: Radius as a function of time, assuming the bolometric luminosities from the middle panel and the temperatures from the top panel. Linear fits are marked by solid lines. In all three panels, measurements for PS1-10awh are in blue, PS1-10ky in red, SCP 06F6 in black, and SN 2010gx in gold.

disappeared by Day 10, whereas the Mg II absorption is still strong (Figure 6). This might be explained by a cooling photosphere, as Mg II has a lower ionization potential (7.6 eV) than C II (11.3 eV) or Si III (16.4 eV). Similarly, the O II lines have become weaker by Day 4, consistent with its rather high ionization potential of 13.6 eV. Also, the source of the line blanketing blueward of 3000 Å remains an interesting mystery, as line blanketing is usually caused by Fe-peak elements, but there are no iron lines apparent in the spectra during or preceding light curve maximum.

5. BOLOMETRIC LUMINOSITY

We totaled up the interpolated flux for PS1-10ky before Day −4 and PS1-10awh after Day −4, and found a radiated energy of $(6.2 \pm 0.7) \times 10^{50}$ erg. This was calculated using trapezoidal interpolation across all observed bands, and linearly extrapolating the integration out to the edges of the observed bands (most importantly, we impose a blue cut-off of 4050 Å to the g_{P1} band in the observer frame). We can perform a similar calculation for the multi-band photometry of SN 2010gx, which covers times after Day −12 and a rest-frame wavelength range of 2600–7300 Å when u -band measurements are included

(SCP 06F6 is not detected in a sufficient number of bands to justify such an analysis). For SN 2010gx we measure a total radiated energy of $(3.7 \pm 0.2) \times 10^{50}$ erg. These are strong lower limits on the total radiated energy because they only represent the measured flux. Not all bands are constrained at all dates, and even when fluxes are constrained at all bands, we are only measuring the SED over a limited wavelength range (~ 2100 – 5300 Å in the rest frame for PS1-10ky and PS1-10awh). Conveniently, the SEDs of SCP 06F6-like objects peak in the ultraviolet, around ~ 2500 Å (e.g., Figures 6 and 7), so despite our limited rest-frame wavelength coverage, we may still be detecting the majority of the radiated energy.

Next, we attempt to more realistically model the bolometric luminosity by accounting for the flux emitted redward of the reddest band measured. The behavior of the SED blueward of the g_{P1} band is poorly understood and clearly diverges from a blackbody (Figure 7), but at redder wavelengths the spectrum can be roughly described as a Planck law. On any given date, we assume a temperature from the polynomial fit to our data (black line in top panel of Figure 8; the actual data imply error bars on temperature that are so large at some times, they preclude a meaningful measurement of bolometric luminosity). We then splice the red tail of a blackbody curve of this temperature onto the reddest constrained photometric point, and sum up the measured photometric points (as described above) with this blackbody tail. Bolometric light curves estimated using this technique are plotted in the middle panel of Figure 8. The bolometric light curves of PS1-10awh and PS1-10ky match up rather well, with maximum luminosities of $(2.3 \pm 0.3) \times 10^{44}$ erg s $^{-1}$ and $(3.0 \pm 0.4) \times 10^{44}$ erg s $^{-1}$ respectively, translating to a bolometric magnitude of -22.5 mag. For SN 2010gx and SCP 06F6, the light curves peak at $(1.8 \pm 0.1) \times 10^{44}$ erg s $^{-1}$ and $(2.0 \pm 0.9) \times 10^{44}$ erg s $^{-1}$ respectively, but bear in mind that these are lower limits. The bolometric light curves are also less symmetrically shaped than the single-band light curves, displaying a slower decline than rise. This is due to the cool temperatures at late times, which imply a larger correction from the red tail of the blackbody curve.

Using this technique, we find an integrated radiated energy of $(8.7 \pm 1.0) \times 10^{50}$ erg for the combined light curve of PS1-10ky and PS1-10awh. This again is likely to be a lower limit, as we are not accounting for any flux blueward of 2100 Å and after Day 16, when the g_{P1} -band flux fades below detectability, we are not accounting for flux blueward of ~ 2850 Å. Similarly, for SN 2010gx we measure $(4.3 \pm 0.2) \times 10^{50}$ erg redward of 2600 Å and after day −5. Finally, we measure a radiated energy of $(5.9 \pm 1.6) \times 10^{50}$ for SCP 06F6; in this case we only measure flux redward of 3150 Å in the rest frame, and between Days −21 and 17 (before Day −21, there are no constraints on the temperature evolution). This technique for estimating bolometric luminosity provides lower limits on all four sources, but these lower limits approach the true bolometric luminosity most closely for PS1-10ky and PS1-10awh, where we have good blue sensitivity out to 2100 Å in the rest frame. For SCP 06F6, assuming a similar color evolution as PS1-10ky/PS1-10awh in the ultraviolet, we are likely

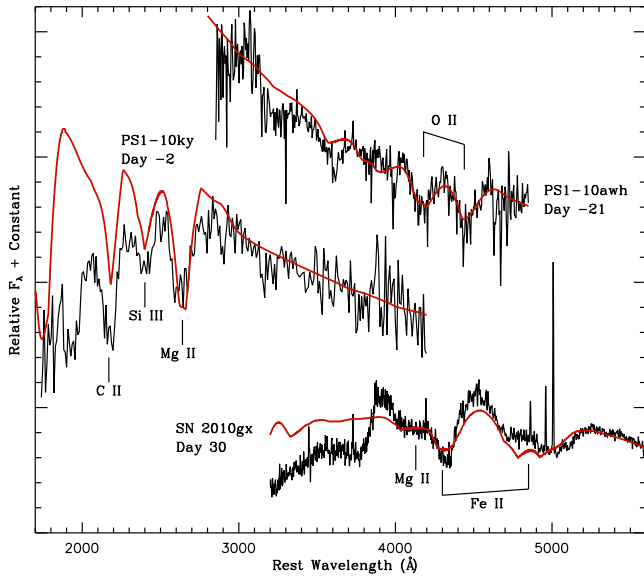


FIG. 9.— SYNOW fits to three spectra are marked as red lines overlying the spectra. The top spectrum is of PS1-10awh on Day -21, and was fit with O II. The middle spectrum is of PS1-10ky on Day -2 and shows the characteristic blue triplet of lines, fit with C II, Si III, and Mg II. The bottom spectrum is SN 2010gx on Day 30, and is fit with Fe II and Mg II.

underestimating its bolometric luminosity by a factor of ~ 2 .

If we assume that these ultra-luminous SNe can be described as blackbodies of the temperatures measured in §4 across their entire spectra (or alternatively, that the line-blanketed blue flux re-emerges at redder wavelengths, conserving the blackbody luminosity), the estimate of the total radiated energy for PS1-10ky/PS1-10awh increases to $(2.6^{+6.2}_{-1.9}) \times 10^{51}$ erg; note the extremely large error bars due to very uncertain temperature determinations on some days. More solid temperature determinations can be made for SN 2010gx, but only after Day -11. We measure a total radiated energy of $(1.0 \pm 0.1) \times 10^{51}$ erg over this limited time range for this source. If instead we use our quadratic fit to the temperature evolution, the integrated radiated energy of PS1-10ky/PS1-10awh is $(1.4 \pm 0.6) \times 10^{51}$ erg, for SN 2010gx it is $(1.1 \pm 0.5) \times 10^{51}$ erg, and the total radiated energy of SCP 06F6 is $(1.6 \pm 0.8) \times 10^{51}$ erg. These can essentially be viewed as upper limits on the radiated energy over the time ranges constrained by observations.

6. EXPANSION VELOCITY

We can constrain the expansion velocity of these SNe by measuring the blueshift of the absorption lines, assuming that their rest frame coincides with the narrow Mg II absorption seen in their spectra (presumably from the host galaxy), and that the lines are identified correctly in Quimby et al. (2011). For spectra with coverage in the blue, we modeled C II, Si II, and Mg II in SYNOW (Jeffery & Branch 1990), with lines formed at an excitation temperature of 10,000 K, a radial power-law distribution of line optical depth proportional to r^{-7} , and a maximum ejecta velocity of $40,000 \text{ km s}^{-1}$. A typical fit is shown as the middle spectrum in Figure 9; clearly there is additional line blanketing that is not being character-

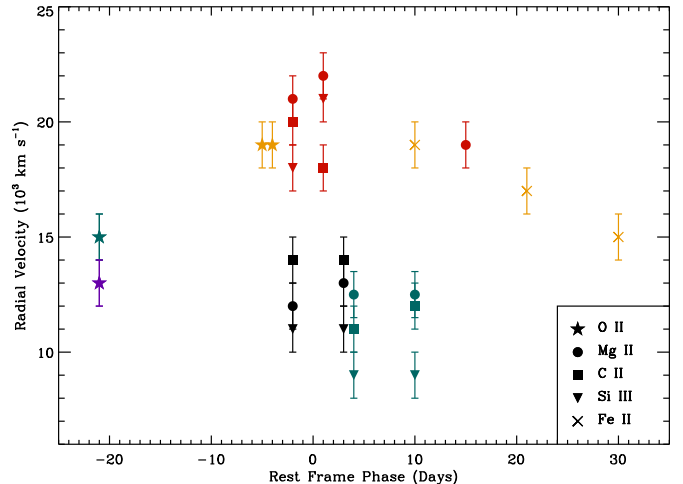


FIG. 10.— Radial velocities measured from absorption lines as a function of rest-frame time relative to light-curve maximum. Measurements for PS1-10awh are in blue, PS1-10ky in red, SCP 06F6 in black, and SN 2010gx in gold. Different absorption lines are denoted by a variety of symbols, as shown in the key at lower right.

ized by the simple SYNOW fit, but the absorption features are roughly reproduced. The central wavelength of each absorption feature is primarily determined by the SYNOW parameter v_{mine} , which signifies the lowest velocity at which a given ion is present in the ejecta. In all cases, values of v_{mine} for C II, Si II, and Mg II agree within 4000 km s^{-1} (Figure 10, and we set the photospheric velocity to the lowest value of v_{mine} found between these three ions. For the expansion velocities quoted in Table 3, we take the average of the three values of v_{mine} . We find expansion velocities measured at absorption minima of $\sim 19,000 \text{ km s}^{-1}$ for PS1-10ky and $\sim 12,000 \text{ km s}^{-1}$ for PS1-10awh and SCP 06F6 (Table 3). A glance at Figure 6 confirms that PS1-10ky is indeed expanding faster than the other two SNe—the three absorption features between $2000\text{--}3000 \text{ Å}$ are noticeably bluer for this source.

For the Day -21 spectrum of PS1-10awh with redder wavelength coverage, we similarly fit the O II “W”-shaped feature in SYNOW, making the same assumptions as above except using an excitation temperature of 13,000 K (Figure 9). We find an expansion velocity of $\sim 15,000 \text{ km s}^{-1}$. We also fit the expansion velocity of SN 2010gx using this feature in the Day -5 and Day -4 spectra, and found a velocity of $\sim 19,000 \text{ km s}^{-1}$ in both cases. Later in the evolution of SN 2010gx, the O II “W”-shaped feature disappears, and we fit the velocity in SYNOW using the broad absorption feature around 4300 Å on Days 10, 21, and 30, describing it with a blend of Fe II and Mg II and assuming basic parameters as described above (bottom spectrum in Figure 9). The spectrum of SCP 06F6 from 2006 April 22 and the spectrum of PS1-10ky from 2010 Sep 9 could not be evaluated, as there are no clear spectral features present (we note that there are no apparent O II features in the SCP 06F6 spectrum from Day -13, while they are clear in the first spectrum of PS1-10awh from Day -21 and the SN 2010gx spectra from Day -5 and Day -4).

As a simple diagnostic of line shape, we also fit the FWHM of each line and take the average if there are

multiple features measured in a spectrum; these are also listed in Table 3. This is certainly an over-simplistic interpretation of the line shapes, as some of the features are blends and therefore they will not necessarily have the same width or structure. Typical spreads in our measurement of FWHM are large, on the order of 3000 km s^{-1} . Line widths are typically $9000\text{--}12,000 \text{ km s}^{-1}$.

PS1-10awh, PS1-10ky, and SCP 06F6 show no evidence for decreasing line velocity with time, displaying similar expansion velocities before and after peak (Table 3 and Figure 10). This is roughly consistent with the bottom panel of Figure 8, where we plot the estimated radii as a function of time, assuming temperatures measured as described in §4 (except in the case of SCP 06F6, where we use the quadratic fit to temperature as a function of time) and luminosities determined from the technique accounting for photometric flux and the red blackbody tail technique in §5. The estimates of radius are very noisy, but growth with time can be fit with a straight line for these three sources, as would be expected for a roughly constant photospheric velocity. The best-fit expansion velocities of the blackbody photospheres are: $10,600 \pm 3800 \text{ km s}^{-1}$ for PS1-10awh, $17,700 \pm 3200 \text{ km s}^{-1}$ for PS1-10ky, $8,600 \pm 400 \text{ km s}^{-1}$ for SN 2010gx, and $11,400 \pm 5700 \text{ km s}^{-1}$ for SCP 06F6. Again we remind the reader that the luminosities used to measure these radii are lower limits—especially in the cases of SN 2010gx and SCP 06F6—and this will translate to underestimates of the expansion velocities. Given the large uncertainties, these velocities measured from radius estimates are consistent with our measurements from the spectral lines.

The behavior of SN 2010gx is more complex, and comparison of its two phases (when it resembles SCP 06F6 and when it resembles a normal Type Ic SN) is complicated by being forced to use different lines with different systematic uncertainties at different times.

The early expansion velocity of $\sim 19,000 \text{ km s}^{-1}$ observed around Day -5 is consistent with the other three sources, but we do not have sufficient spectroscopic information during this SCP 06F6-like phase to discern if it is constant. Later, when SN 2010gx shows Fe II indicative of a Type Ic SN, its photospheric velocity shows evidence of deceleration from $19,000 \text{ km s}^{-1}$ on Day 10 to $15,000 \text{ km s}^{-1}$ on Day 30 (also apparent in Figure 6). We note that comparisons of velocities measured from different features should be carried out cautiously, as some absorption features may actually be blends of ions that are not properly accounted for in our *SYNOW* modeling, introducing uncertainty into absolute velocity measurements (therefore, it is difficult to state with certainty that the photospheric velocity of SN 2010gx was constant between Day -5 and Day 10). However, relative comparisons of velocities measured using the same features should be reliable. Therefore, the data are consistent with constant radial velocity in PS1-10ky, PS1-10awh, and SCP 06F6, and provide evidence for decreasing velocity in the latter SN Type Ic phase of SN 2010gx.

Our analysis for these four ultra-luminous SNe implies that while they are in an SCP 06F6-like phase, showing a relatively featureless continuum with a few broad absorption lines of lighter metals, they do not show any clear sign of change in the rate of photospheric expansion. This apparent lack of deceleration is in direct con-

trast with SN 2005ap, where the “W”-shaped feature is observed to decelerate by $4,000 \text{ km s}^{-1}$ over seven days in the rest frame (Quimby et al. 2007). The apparently constant velocities measured for PS1-10ky, PS1-10awh, and SCP 06F6 are mostly measured from the blue lines of C II, Mg II, and Si III; it is possible that these lines form at a significantly different location in the photosphere from the O II “W”-shaped feature, and may therefore show different velocity evolution. SN 2010gx hints that, later in the evolution of these ultra-luminous SNe, the measured velocities will decline, as typically observed during the photospheric phase of SN expansion, while the photosphere recedes into progressively slower-moving ejecta.

7. MODELS FOR SCP 06F6-LIKE SNE

In this section we consider three physical scenarios that have been proposed to explain ultra-luminous SNe. We compare the predictions of these models with the data presented above, in an effort to define the parameter space that these objects may inhabit. When we discuss bolometric light curves, we are using the luminosities calculated by totaling up the flux in the observed bands and adding on the red tail of a blackbody fit, as described in §5 and plotted in Figure 8. These are likely to be slight underestimates of the true bolometric luminosity for PS1-10awh and PS1-10ky, but they are the best estimate we can make given our limited wavelength coverage.

7.1. Scenario 1: Radioactive Decay

Free from the H-envelopes associated with most Type II SNe, the photospheric emission from Type I SNe is powered by the radioactive decay of freshly synthesized ^{56}Ni and ^{56}Co within the ejecta. The associated optical signal reaches maximum intensity within a month of the explosion at which point the photons diffuse efficiently out of the optically-thick layers causing the light curve to decay. The characteristic time of photon diffusion, $\tau_c \propto M_{\text{ej}}^{3/4} E_K^{-1/4}$ days, is determined by fundamental ejecta properties (Arnett 1982): the total mass (M_{ej} ; in units of M_\odot) and the kinetic energy (E_K ; in units of $10^{51} \text{ erg s}^{-1}$). As originally shown by Phillips (1993) for SNe Ia and Valenti et al. (2008) and Drout et al. (2010) for SNe Ibc, the post-maximum decay rate may serve as a proxy for the light-curve width since broader light-curves are associated with slower decline rates. We adopt the notation, Δm_{15} , which represents the magnitude decrease in the 15 days following the peak luminosity.

The peak luminosity (L_{peak}) is primarily determined by the mass of ^{56}Ni (M_{Ni} ; see Arnett 1982). Meanwhile, spectroscopic measurements of the photospheric velocity (v_{ph}) directly constrain the quantity $\sqrt{E_K/M_{\text{ej}}}$, thus enabling all three physical parameters (M_{Ni} , E_K , and M_{ej}) to be determined uniquely based on three observables: (i) the peak luminosity, (ii) the light-curve width, and (iii) the velocity of the photosphere.

For the rest-frame lightcurve of PS1-10ky, we measure a peak bolometric luminosity of $L_{\text{peak}} \approx 3.0 \times 10^{44} \text{ erg s}^{-1}$ and a post-maximum decay rate of $\Delta m_{15} \approx 0.52 \text{ mag}$. Based on theoretical models for Type Ic SN light-curves (Valenti et al. 2008), this decay rate implies a characteristic time of $\tau_c \approx 14$ days and a radioactive mass of $M_{\text{Ni}} \approx 14 M_\odot$. With the photospheric velocity

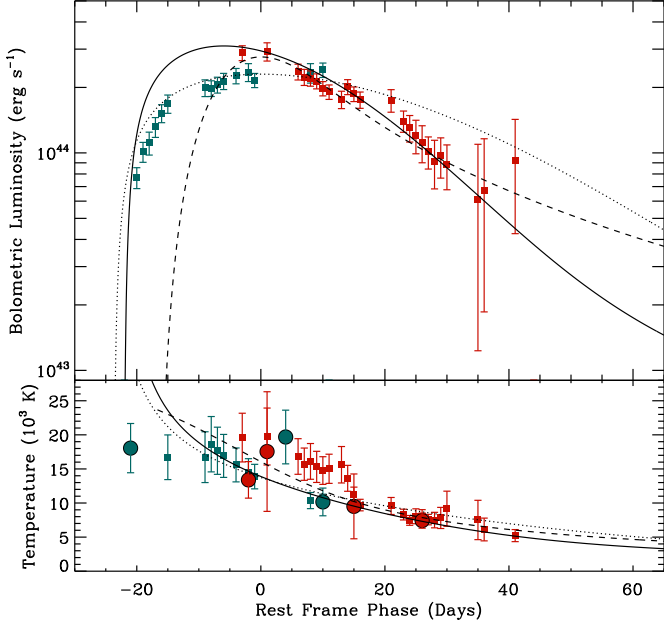


FIG. 11.— Top Panel: Combined bolometric light curve for PS1-10awh and PS1-10ky (colors and symbols as in Fig. 8) fit using magnetar spin-down models (Kasen & Bildsten 2010). Different lines correspond to fits for different SN ejecta masses: $M_{ej} = 1 M_{\odot}$ (dashed), $4 M_{\odot}$ (solid), and $10 M_{\odot}$ (dotted); see text for more details. Bottom Panel: temperature evolution plotted as in Fig 8, with the effective temperature of the magnetar spin-down models overplotted as lines as in the top panel.

of $v_{ph} \approx 18,000 \text{ km s}^{-1}$ measured for PS1-10ky, we estimate $M_{ej} \approx 4.4 M_{\odot}$ and $E_K \approx 8.9 \times 10^{51} \text{ erg}$. This ejecta mass is much less than the nickel mass, implying that a model where radioactive decay powers the bulk of the light curve is unphysical. This is consistent with the findings of Chatzopoulos et al. (2009) and Quimby et al. (2011).

At later epochs ($\Delta t \approx 60 - 300$ days), energy generation within a normal SN’s ejecta is dominated by the radioactive decay of ^{56}Co (half-life $\tau = 77$ days). Late-time light-curves can thus directly probe the mass of radioactive decay products, enabling an independent constraint on M_{Ni} . To date, there has been no late-time photometry of any SCP 06F6-like source, but the appearance of SN 2010gx as a fairly typical SN Ic at late times implies that such an extended tail should exist to the light curve at a low level. Photometric constraints from 76 days after light curve peak place limits on the ^{56}Ni mass ejected by SN 2010gx of $\lesssim 1 M_{\odot}$ (Pastorello et al. 2010). Late-time observations of PS1-10awh on 29 June 2011 (Day 176) imply a 3σ i_{P1} -band limit of >23.7 mag, corresponding to a rough limit on the nickel mass of $M_{Ni} \lesssim 13 M_{\odot}$. At $z \approx 1$, $1 M_{\odot}$ of radioactive material would translate to an i -band magnitude of 26.5 mag at day ~ 100 –150 (rest frame), detectable with deep space-based imaging.

7.2. Scenario 2: Magnetar Spin-Down

Kasen & Bildsten (2010, henceforth KB10) and Woosley (2010) have shown that the spin-down of a magnetar can explain the ultra-luminous SNe with broader light curves and slower decays like SN 2005ap (Quimby et al. 2007) and SN 2008es (Gezari et al. 2009;

Miller et al. 2009). However, it remains unclear if they can fit the relatively narrow symmetric light curves of the SCP 06F6-like objects presented here. We use the formalism of KB10 to model SN light curves powered by magnetar spin-down. The magnetar has a rotational energy $E_p = 2 \times 10^{50} P_{10}^{-2}$ ergs, where P_{10} is its period in units of 10 ms (maximal spin corresponds to ~ 1 ms). The spin-down timescale due to magnetic dipole radiation is $t_p = 1.3 B_{14}^{-2} P_{10}^2 \text{ yr}$, where B_{14} is the magnetar magnetic field strength in units of 10^{14} G . It spins down as $L_p(t) = [E_p(l-1)]/[t_p(1+t/t_p)^l]$, where t is the time since birth, L_p is the energy the magnetar is depositing into the SN ejecta per unit time, and l is an index that describes the magnetar spin-down ($l = 2$ for magnetic dipole spin-down). The velocity of the SN ejecta is $v_{ej} = [2(E_p + E_{SN})/M_{ej}]^{1/2}$, where E_{SN} is the SN explosion energy and M_{ej} is the SN ejecta mass. Finally, the diffusion timescale is $t_d = [(3M_{ej}\kappa)/(4\pi v_{ej}c)]^{1/2}$, where κ is the opacity in $\text{cm}^2 \text{ g}^{-1}$ and c is the speed of light.

Using these definitions, we solve for the emitted luminosity L_e with the differential equation:

$$\frac{\partial L_e(t)}{\partial t} = \frac{E_p(l-1)t}{t_d^2 t_p(1+t/t_p)^l} - \frac{t L_e(t)}{t_d^2} \quad (2)$$

and then multiply the luminosity by a correction factor $(l+1)/2$ as prescribed by KB10. Using this simple technique, the time to peak luminosity also differs from that solved for in hydrodynamic simulations by KB10. We use their Equation 16 to solve for the “correct” peak time, and then scale the time axis of our light curve so that the peak time produced by our equation 2 matches it. We find that we can match the published light curves in KB10 well with these simple assumptions.

We leave fixed $l = 2$, $\kappa = 0.2 \text{ cm}^2 \text{ g}^{-1}$ (as assumed by KB10), and $E_{SN} = 10^{51} \text{ erg}$; we vary P_{10} , B_{14} , and M_{ej} . The bolometric light curve for PS1-10awh and PS1-10ky can be matched reasonably well with $B_{14} = 2.7$, $P_{10} = 0.16$, and $M_{ej} = 4 M_{\odot}$, represented as the solid line in Figure 11. We recognize that the light curves for PS1-10awh and PS1-10ky do not match up perfectly, so PS1-10awh is only used as a rough constraint on the rise time. The magnetar in such a model dominates the SN energy with a rotational energy of $8 \times 10^{51} \text{ erg}$, and the swept-up shell will expand at $14,900 \text{ km s}^{-1}$, also in good accord with measured expansion velocities.

We can also perform a rough comparison with our observed temperature evolution by calculating the effective temperatures of the magnetar models $T = [L_e/(4\pi\sigma v_{ej}^2 t^2)]^{1/4}$ where σ is the Stefan-Boltzmann constant. We plot the predicted temperature evolution in the bottom panel of Figure 11, and find that it is consistent with our data.

The light curve can be fit with a range of ejecta masses, from 2 – $5 M_{\odot}$. For lower ejecta masses, P_{10} must increase and B_{14} must decrease to fit the data. For example, the best match for $M_{ej} = 3 M_{\odot}$ is $B_{14} = 2.5$ and $P_{10} = 0.20$ (implying an expansion velocity of $14,200 \text{ km s}^{-1}$), while for $M_{ej} = 5 M_{\odot}$ the data can be described well with $B_{14} = 3.4$, $P_{10} = 0.11$ (giving a velocity of $18,800 \text{ km s}^{-1}$). In Figure 11, we show two additional models that illustrate why the range of well-fit ejecta masses is limited. The dotted line shows a light curve that matches

the peak bolometric luminosity for $M_{\text{ej}} = 10 M_{\odot}$; clearly the late-time decline of the light curve is too gradual. This lack of good fit for high M_{ej} is due to the maximal spin of a magnetar at $P_{10} = 0.1$ (KB10). There is also no good fit to the light curve for $M_{\text{ej}} = 1 M_{\odot}$ (dashed line), as a model that produces appropriate peak luminosity and light curve decline also predicts a light curve rise that is far too rapid. We therefore conclude that PS1-10ky and PS1-10awh can be plausibly fit with ejecta masses of $2 - 5 M_{\odot}$, spanning the commonly observed range of ejecta masses for SNe Type Ic (Drout et al. 2010). Different ejecta masses might explain the measured differences in expansion velocity.

The KB10 magnetar model also makes the distinct prediction that the SN photospheric velocity should be constant with time, consistent with our observations (Table 2.2). This is because the magnetar blows a hot low-density bubble in the center of the SN, producing a dense fast-moving shell that sweeps up the ejecta. Unlike in a normal SN, where the photosphere recedes inward to ejecta with slower velocities, the photosphere stalls at this dense shell in the magnetar model, implying a roughly constant observed expansion velocity. However, it is possible that the magnetar spin-down model would struggle to produce late-time SN Ic emission as seen in SN 2010gx, for this very same reason: the magnetar has cleared out a low-density bubble around it, and the ejecta are no longer expanding homologously but as a relatively thin shell. We also note that the measured evolution of the radius (Figure 8) is consistent with a shell that begins expanding at constant velocity from a very small radius around Day -40 or Day -30 , roughly coincident with the first detections of SCP 06F6-like sources; however, our radius calculations are very uncertain, and better temperature determinations before light curve maximum are required to constrain the radius at early times.

7.3. Scenario 3: Shock Breakout and Circumstellar Interaction

The extremely high radiated energies of many ultra-luminous SNe has been explained by interaction with a dense circumstellar medium (CSM). The general idea is that interaction with CSM transforms much of the SN's kinetic energy into radiation before it can be lost to adiabatic expansion (e.g., Smith & McCray 2007; Chevalier & Irwin 2011).

Chevalier & Irwin (2011, henceforth CI11) propose that the light curves of SCP 06F6 and related objects might be explained by shock breakout from a dense but truncated CSM. A stellar wind with mass loss rate \dot{M} and velocity v_w is expelled from the SN progenitor for a time t_{ml} before the SN explosion, producing a $\rho \propto r^{-2}$ density profile that abruptly drops to zero for radii greater than $r_w = t_{\text{ml}} v_w$. If the diffusion radius of the SN (r_d) is roughly equivalent to the radius of this stellar wind, SN energy will be transformed into radiation very efficiently, resulting in a luminous burst of radiation with a fairly symmetric light curve. We can use our measured peak bolometric luminosity ($L_{\text{peak}} = 3.0 \times 10^{44} \text{ erg s}^{-1}$) and peak temperature ($T_{\text{peak}} = 14,700 \text{ K}$) to measure this radius ($r_w = 3.0 \times 10^{15} \text{ cm}$). From the PS1-10ky/PS1-10awh light curve, we estimate a rise time of $t_d \approx 25$ days, which can be roughly equated to the diffusion time

t_d :

$$t_d = 6.6 k D_{\star} \text{ days} \quad (3)$$

where k is the opacity in units of $0.34 \text{ cm}^2 \text{ g}^{-1}$ and D_{\star} parameterizes the mass loss in the stellar wind as $D_{\star} = (\dot{M}/10^{-2} M_{\odot})(v_w/10 \text{ km s}^{-1})$. For an ionized He-rich wind, $k=0.59$ and we find $D_{\star} = 6.4$. Integrating this density profile out to r_w , we find that the total mass in the stellar wind is $6.1 M_{\odot}$. Assuming a Wolf-Rayet (W-R) progenitor star with $v_w = 1000 \text{ km s}^{-1}$ (Nugis & Lamers 2000), this corresponds to a wind powered for approximately one year at a mass loss rate $\dot{M} = 6 M_{\odot} \text{ yr}^{-1}$.

Such a mass loss event, expelling several solar masses in the year before stellar death, is extreme, although such episodes are seen for luminous blue variables (LBVs; e.g., Davidson & Humphreys 1997; Smith & Owocki 2006). Pastorello et al. (2007) discovered such an outburst preceding the type Ib SN 2006jc by two years; they attempt to reconcile the LBV-like outburst with the W-R progenitor of the SN, but point out that no such outburst has ever been observed for a W-R star. They conclude that perhaps the W-R progenitor is in a binary with a LBV, or perhaps such outbursts on W-R stars are exceedingly rare. Meanwhile, Foley et al. (2007) point out that a dense He-rich CSM is required to explain the bright He I emission lines in SNe 1999cq, 2002ao, and 2006jc, and hypothesize that perhaps LBV-like eruptions can persist into the WR stage. However, X-ray measurements of SN 2006jc imply that the CSM may not be particularly massive (of order $0.01 M_{\odot}$; Immler et al. 2008), and therefore an episode like that seen in SN 2006jc would need to be significantly scaled up to explain SCP 06F6-like sources.

Given the integrated radiated energy of our combined light curve and k and D_{\star} as described above, we can use Equation 5 from CI11 to find that $E_{51}^2 / M_{\text{ej},10} = 17$, where E_{51} is in units of 10^{51} erg and $M_{\text{ej},10}$ is in units of $10 M_{\odot}$. For an ejecta mass of $10 M_{\odot}$, this implies a SN energy of $4.1 \times 10^{51} \text{ erg}$. We can also solve for the diffusion radius using Equation 3 from CI11 and find $r_d = 1.4 \times 10^{15} \text{ cm}$, similar to r_w within a factor of two and implying that these objects are in the $r_w \approx r_d$ regime where radiation is produced most efficiently.

The inner ejecta of a SN explosion typically have a rather flat density profile ($\rho_{\text{in}} \propto r^{-1}$ or constant), while the density of the outermost ejecta falls off much more steeply ($\rho_{\text{out}} \propto r^{-7}$). The CI11 model assumes that the reverse shock is evolving into the steep outer part of the density profile, but this is only true if $E_{51}^{0.5} M_{\text{ej},10}^{-1.5} D_{\star} t_{\text{SN}} < 320$, where t_{SN} is the age of the SN in days. At the beginning of shock breakout, $t_{\text{SN}} = t_d$ and this condition is marginally satisfied. As shock breakout proceeds, the reverse shock will proceed toward the flatter part of the density profile. Assuming an ejecta mass of $10 M_{\odot}$, the expanding shell will contain $2.3 M_{\odot}$ swept up from the circumstellar medium and $1.3 M_{\odot}$ of reverse-shocked ejecta. This shell will contain $2/3 E_{51}$, implying a shell velocity of $9,000 \text{ km s}^{-1}$, which is lower than we observe. The lower ejecta masses necessary to produce higher velocities imply $E_{51}^{0.5} M_{\text{ej},10}^{-1.5} D_{\star} t_{\text{SN}} > 320$ at t_d , requiring a model for circumstellar interaction that takes into account both the ρ_{out} and ρ_{in} regimes of the ejecta density profile. The development of such a model

is outside the scope of this work, but the ejecta velocities measured here (especially the high values measured for SN 2010gx and PS1-10ky) will provide important future constraints.

Smith & McCray (2007) propose a scenario similar to CI11 to explain the light curve of SN 2006gy. However, in their model the SN shock does not break out of an r^{-2} smooth wind, but rather plows into an optically-thick shell. The exact density profile of the CSM will not change the light curve significantly, as the light curve is largely determined by simply the radius and mass of the surrounding material. Therefore, the Smith & McCray model give results similar to those derived above using CI11.

The same basic physics also operates in the pulsational pair instability model (Woosley et al. 2007), favored by Quimby et al. (2011) to explain their SCP 06F6-like sources. In this scenario, a massive star has not yet exploded and died, but in approaching the end of its life violently ejects massive shells (some as massive as $18 M_{\odot}$) that collide with one another and produce luminous outbursts. Some of the theoretical light curves feature rather steep declines reminiscent of the SCP 06F6-like sources. However, the Woosley et al. (2007) model struggles to produce outbursts with velocities significantly in excess of $\sim 5,000 \text{ km s}^{-1}$, even for a massive progenitor star of $130 M_{\odot}$. We therefore find pulsational pair-instability SNe to be an unlikely model for PS1-10awh, PS1-10ky, and SCP 06F6. We also note that such a model does not naturally account for the SN Type Ic features seen in SN 2010gx at late times.

The shock breakout scenario also predicts that the temperature will rise until luminosity maximum, and then decline after maximum (Ensmann & Burrows 1992, CI11). Our temperature measurements (Figure 8) do not clearly follow this trend, appearing to be declining or flat before peak, although these early measurements are extremely noisy. Early detection and deep multi-band photometry will be required in the future to test this prediction of the shock breakout model in additional sources. It is also worth noting that the magnetar model makes a similar prediction for the temperature evolution (KB10), so early-time temperature measurements are unlikely to distinguish between the two models.

We also note that the definition of temperature becomes complex for the non-equilibrium conditions involved in shock breakout. Numerous works (e.g., Ensmann & Burrows 1992; Katz et al. 2010; Nakar & Sari 2010) find that the radiation or color temperature of the shock breakout emission is higher than the effective temperature (defined by the luminosity surface density $L/4\pi r^2$). If this holds true in the case of SCP 06F6-like objects, it would increase the wind radius calculated here. The total mass expelled by the progenitor in a wind would increase, but other parameters like D_{\star} and $E_{51}^2 / M_{\text{ej},10}$ would not be affected. Such a discrepancy may be necessary if the shock breakout model holds true, as the SN is predicted to expand for a time t_d before the light curve begins to rise (CI11). However, our measured radii (Figure 8) are consistent with explosion at approximately Day -30 , around the time the light curves begin to rise. A decrease in effective temperature by $\sim 40\%$ (consistent with that predicted by Ensmann & Burrows 1992) could

increase the blackbody radii and provide space for expansion that begins at Day -60 rather than Day -30 .

Also interesting within the shock breakout picture is the fact that the expansion velocities do not appear to decline over ~ 30 day baselines (§6). This might naturally be explained if, indeed, there is no CSM outside of the diffusion radius and therefore the shock is not undergoing any deceleration. However, this is perhaps an oversimplification, as we note that the bolometric light curve for PS1-10awh and PS1-10ky shows some indication of a late-time tail (§5, Fig 8) and we calculate r_w to be slightly larger than r_d . There is therefore the possibility of ongoing CSM interaction at later times, complicating our simple shock breakout picture from a truncated CSM. However, we must remember that these observations are sensitive to an uncertain temperature evolution and they are the product of two independent light curves which have been spliced together.

7.3.1. Predicted Radio Emission

We can predict the radio signature for such a shock breakout from a dense wind using standard models of radio SNe (Chevalier 1996). While the shock front is inside r_d , it propagates as a radiation-dominated shock wave. This shock structure does not give rise to particle acceleration to relativistic energies, so no radio synchrotron emission will result in this early stage. If $r_w > r_d$ and the blast wave continues to interact with CSM after breakout, some particle acceleration might occur, but it would likely result in a relatively short-lived burst of radio emission, as r_w can not be significantly larger than r_d if we are to explain the very high luminosities of SCP 06F6-like objects and the large drop from maximum observed in some objects (e.g., SN 2010gx). In addition, any radio emission will be heavily absorbed due to free-free processes (Weiler et al. 2002) and synchrotron self absorption (Chevalier 1998), so any burst of radio emission will to be faint.

If the stellar wind is truncated as described above, the SN will then expand past the CSM. Even if relativistic particles and magnetic field had been present, their energy densities would rapidly decline due to adiabatic expansion, and the radio flux density would plummet as $S_{\nu} \propto t^{-6}$ (Shklovskii 1960). It is possible at this point that a viscous reverse shock develops, but the reverse shock is less powerful than the forward shock, the magnetic field is likely to be weak, and any accelerated particles are subject to loss processes (Coulomb, inverse Compton, and/or synchrotron), so that the reverse shock is unlikely to be a strong source of synchrotron emission. Therefore, after the shock expands past r_w , it is unlikely to be a source of radio emission; our EVLA non-detections are not surprising in light of this model.

Finally, we note that we do not expect bright radio emission from the magnetar spin-down scenario (§7.2). Even Galactic magnetars are typically not detected at radio wavelengths (e.g., Gaensler et al. 2001; Burgay et al. 2006), and the new-born magnetars proposed by KB10 will additionally suffer free-free absorption from the ionized ejecta in which they are embedded. We therefore do not expect SCP 06F6-like objects to be sources of radio emission, but only the future combination of deep optical time-domain searches with the Large Synoptic Survey Telescope (LSST; Ivezić et al. 2008) and accompanying

blind radio transient surveys with the Australian Square Kilometre Array Pathfinder (ASKAP; Johnston et al. 2007) will fully test this hypothesis.

8. CONCLUSIONS

Using multi-color photometry and multi-epoch spectroscopy, we find that SCP 06F6-like objects radiate $\sim 10^{51}$ erg in just a few months, making them amongst the most energetic SNe known. Their peak bolometric magnitudes are typically $\lesssim -22.5$ mag, as compared with -19.5 mag for SNe Type Ia (Contardo et al. 2000), -21.4 mag for the proposed pair-instability SN 2007bi (Gal-Yam et al. 2009; Young et al. 2010), and -21.8 mag for the ultra-luminous Type IIn SN 2006gy (Smith et al. 2007; Ofek et al. 2007). Our estimates are consistent with the lower-redshift sources presented in Quimby et al. (2011).

There is no evidence for decreasing radial velocity during the SCP 06F6-like phase in the objects studied here, consistent with the expansion of an optically-thick shell predicted by both the magnetar and circumstellar interaction scenarios. However, the SCP 06F6-like SN 2005ap provides a counter-example to this point, displaying a clear decrease in velocity (Quimby et al. 2007). A larger sample of objects with time-series spectroscopy is required to test the prevalence of decelerating photospheric velocities in SCP 06F6-like objects. One source to date, SN 2010gx (Pastorello et al. 2010) has shown evidence for dissipation of the optically-thick shell and a decrease in optical depth, revealing a normal SN Type Ic in its interior.

Here, we show that radioactive decay can not explain SCP 06F6-like objects, which rules out pair-instability models (e.g., Barkat et al. 1967) for this particular class of ultra-luminous SNe, unlike in the case of the unusually luminous SN 2007bi (Gal-Yam et al. 2009). We investigate two physical scenarios that both require an energetic optically-thick shell: the spin-down of a new-born magnetar or shock breakout from a dense circumstellar medium. Both scenarios can fit our data with plausible parameters for a SN Type Ic, although both require rather extreme additional conditions. If magnetars are responsible for SCP 06F6-like objects, they need to be spinning near breakup (1 – 2 ms period). Meanwhile, if shock breakout causes these events, the progenitor must have undergone an LBV-like outburst, expelling several solar masses of H-poor material in just a few years before stellar death; however, no such violent eruption has ever been observed from the Wolf-Rayet stars that are likely the progenitors of these SNe (although dense Herich CSM has been observed to be present around some SNe Type Ib; Pastorello et al. 2007; Foley et al. 2007). One of the most promising strategies for distinguishing between these scenarios in the future is early-time measurement of the photospheric radius, because at the time of light curve rise in the CSM interaction model, the SN will expand from a relatively much larger radius as compared with the magnetar spin-down model. In addition, late-time observations have the potential to distinguish between the two models. For example, the later observations of SN 2010gx may conflict with expectations from the magnetar model, as this scenario predicts that the SN ejecta themselves are being swept into a thin shell by the magnetar wind; however, relatively normal SN Type

Ic ejecta are observed in this source at late times.

Any model for SCP 06F6-like sources needs to explain why these ultra-luminous events are only associated with a small fraction of SN explosions; the extreme conditions implied by both models discussed here might justify their rarity, but it remains to be determined if we can expect such fast-spinning magnetars or dense H-poor circumstellar media in sufficient numbers to explain the rates of SCP 06F6-like sources. The lack of detection of host galaxies for PS1-10ky and PS1-10awh (down to $0.02 L^*$) implies that they are in dwarf galaxies with low metallicities and high specific SFRs. This is a common feature for these type of transients (Quimby et al. 2011; Pastorello et al. 2010; Neill et al. 2011). As none have been found in an L^* -type galaxy, this may point to metallicity playing a key role in the progenitor channel—or it may simply be an artifact of the bulk of cosmic star formation occurring in systems with high specific SFR. A larger sample of SCP 06F6-like sources is required to distinguish between these scenarios.

Moreover, we note that these sources display some degree of homogeneity as a class, showing peak luminosities, expansion velocities, and temperature evolution which agree to better than a factor of two across our (albeit small) sample. Given the widespread cut-off in luminosity blueward of 2500 \AA , we believe SCP 06F6-like sources will be of limited utility for ultraviolet high-redshift absorption-line studies (e.g., Ly α), in contrast with the claims of Quimby et al. (2011). As wide-field surveys like PS1 and PTF continue to operate, many more SCP 06F6-like sources will be discovered; PS1 is currently discovering ~ 1 such source each month at $z \gtrsim 0.5$. We will be able to test their diversity as a class and measure their rates. Increased sample sizes at a range of redshifts will better constrain the physical properties of these highly energetic explosions, their host stellar populations, and discern between the magnetar spin-down and shock breakout scenarios.

9. ACKNOWLEDGMENTS

We would like to thank Dan Kasen and Shmuel Balberg. Laura Chomiuk is a Jansky Fellow of the National Radio Astronomy Observatory. Ryan J. Foley is supported by a Clay Fellowship. This discovery was enabled using the PS1 System operated by the PS1 Science Consortium (PS1SC) and its member institutions. The PS1 Surveys have been made possible through the combinations of the Institute for Astronomy at the University of Hawaii, The Pan-STARRS Project Office, the Max-Planck Society and its participating institutes, the Max Planck Institute for Astronomy, Heidelberg, and the Max Planck Institute for Extraterrestrial Physics, Garching, The Johns Hopkins University, the University of Durham, the University of Edinburgh, the Queen's University of Belfast, the Harvard-Smithsonian Center for Astrophysics, the Las Cumbres Observatory Global Network, and the National Central University of Taiwan. Observations reported here were obtained at the MMT Observatory, a joint facility of the Smithsonian Institution and the University of Arizona. This paper uses data products produced by the OIR Telescope Data Center, supported by the Smithsonian Astrophysical Observatory. The EVLA is run by the National Radio Astronomy Observatory, a facility of the National Sci-

ence Foundation operated under cooperative agreement by Associated Universities, Inc. Gemini Observatory is operated by the Association of Universities for Research in Astronomy, Inc., under a cooperative agreement with the NSF on behalf of the Gemini partnership: the National Science Foundation (United States), the Science and Technology Facilities Council (United Kingdom), the National Research Council (Canada), CONICYT (Chile), the Australian Research Council (Australia), Ministério da Ciência e Tecnologia (Brazil) and

Ministerio de Ciencia, Tecnología e Innovación Productiva (Argentina). We are grateful for access to Gemini under programs GN-2010A-Q-30 and GS-2010B-Q-4 (PI: E. Berger) and GN-2010B-Q-34 (PI: J. Tonry). Partial support for this work was provided by National Science Foundation grants AST-1009749 and AST-0807727.

Facilities: PS1(GPC1), MMT (Blue Channel Spectrograph, Hectospec), Gemini:Gillett (GMOS), EVLA, GALEX

REFERENCES

- Abazajian, K. N., et al. 2009, *ApJS*, 182, 543
 Arnett, W. D. 1982, *ApJ*, 253, 785
 Barbary, K., et al. 2009, *ApJ*, 690, 1358
 Barkat, Z., Rakavy, G., & Sack, N. 1967, *Physical Review Letters*, 18, 379
 Burgay, M., Rea, N., Israel, G. L., Possenti, A., Burderi, L., di Salvo, T., D’Amico, N., & Stella, L. 2006, *MNRAS*, 372, 410
 Cardelli, J. A., Clayton, G. C., & Mathis, J. S. 1989, *ApJ*, 345, 245
 Chatzopoulos, E., Wheeler, J. C., & Vinko, J. 2009, *ApJ*, 704, 1251
 Chevalier, R. A. 1996, in *ASP Conf. Ser.*, Vol. 93, *Radio Emission from the Stars and the Sun*, ed. A. R. Taylor & J. M. Paredes, 125
 Chevalier, R. A. 1998, *ApJ*, 499, 810
 Chevalier, R. A., & Irwin, C. M. 2011, *ApJ*, 729, L6
 Christensen, L., Hjorth, J., & Gorosabel, J. 2004, *A&A*, 425, 913
 Contardo, G., Leibundgut, B., & Vacca, W. D. 2000, *A&A*, 359, 876
 Davidson, K., & Humphreys, R. M. 1997, *ARA&A*, 35, 1
 Drout, M. R., et al. 2010, *arXiv* 1011.4959
 Ensmann, L., & Burrows, A. 1992, *ApJ*, 393, 742
 Faber, S. M., et al. 2007, *ApJ*, 665, 265
 Fabricant, D., et al. 2005, *PASP*, 117, 1411
 Foley, R. J., Smith, N., Ganeshalingam, M., Li, W., Chornock, R., & Filippenko, A. V. 2007, *ApJ*, 657, L105
 Frail, D. A., Soderberg, A. M., Kulkarni, S. R., Berger, E., Yost, S., Fox, D. W., & Harrison, F. A. 2005, *ApJ*, 619, 994
 Gaensler, B. M., Slane, P. O., Gotthelf, E. V., & Vasisht, G. 2001, *ApJ*, 559, 963
 Gal-Yam, A., et al. 2009, *Nature*, 462, 624
 Gänsicke, B. T., Levan, A. J., Marsh, T. R., & Wheatley, P. J. 2009, *ApJ*, 697, L129
 Gezari, S., et al. 2009, *ApJ*, 690, 1313
 Hodapp, K. W., Siegmund, W. A., Kaiser, N., Chambers, K. C., Laux, U., Morgan, J., & Mannery, E. 2004, in *SPIE Conf. Ser.*, ed. J. M. Oschmann Jr., Vol. 5489, 667
 Hook, I. M., Jørgensen, I., Allington-Smith, J. R., Davies, R. L., Metcalfe, N., Murowinski, R. G., & Crampton, D. 2004, *PASP*, 116, 425
 Immler, S., et al. 2008, *ApJ*, 674, L85
 Ivezić, Z., et al. 2008, *arXiv* 0805.2366
 Jeffery, D. J., & Branch, D. 1990, in *Supernovae*, Jerusalem Winter School for Theoretical Physics, ed. J. C. Wheeler, T. Piran, & S. Weinberg, 149
 Johnston, S., et al. 2007, *PASA*, 24, 174
 Kaiser, N., et al. 2010, in *SPIE Conf. Ser.*, Vol. 7733, *SPIE Conf. Ser.*, ed. L. M. Stepp, R. Gilmozzi, & H. J. Hall
 Kasen, D., & Bildsten, L. 2010, *ApJ*, 717, 245
 Katz, B., Budnik, R., & Waxman, E. 2010, *ApJ*, 716, 781
 Kennicutt, Jr., R. C. 1998, *ARA&A*, 36, 189
 Kewley, L. J., Geller, M. J., & Jansen, R. A. 2004, *AJ*, 127, 2002
 Kocevski, D., & West, A. A. 2011, *ApJ*, 735, L8+
 Kulkarni, S. R., et al. 1998, *Nature*, 395, 663
 Le Floc’h, E., et al. 2003, *A&A*, 400, 499
 MacFadyen, A. I., & Woosley, S. E. 1999, *ApJ*, 524, 262
 Magnier, E. 2006, in *Proceedings of The Advanced Maui Optical and Space Surveillance Technologies Conference*, ed. S. Ryan, The Maui Economic Development Board, E50
 Mahabal, A. A., & Drake, A. J. 2010, *The Astronomer’s Telegram*, 2508
 Mahabal, A. A., et al. 2010, *The Astronomer’s Telegram*, 2490
 Mannucci, F., Salvaterra, R., & Campisi, M. A. 2011, *MNRAS*, 414, 1263
 Miller, A. A., et al. 2009, *ApJ*, 690, 1303
 Mink, D. J., Wyatt, W. F., Caldwell, N., Conroy, M. A., Furesz, G., & Tokarz, S. P. 2007, in *ASP Conf. Ser.*, Vol. 376, *Astronomical Data Analysis Software and Systems XVI*, ed. R. A. Shaw, F. Hill, & D. J. Bell, 249
 Nakar, E., & Sari, R. 2010, *ApJ*, 725, 904
 Neill, J. D., et al. 2011, *ApJ*, 727, 15
 Nugis, T., & Lamers, H. J. G. L. M. 2000, *A&A*, 360, 227
 Ofek, E. O., et al. 2007, *ApJ*, 659, L13
 Onaka, P., Tonry, J. L., Isani, S., Lee, A., Uyeshiro, R., Rae, C., Robertson, L., & Ching, G. 2008, in *SPIE Conf. Ser.*, Vol. 7014
 Pastorello, A., et al. 2010, *ApJ*, 724, L16
 —. 2007, *Nature*, 447, 829
 Phillips, M. M. 1993, *ApJ*, 413, L105
 Quimby, R. M., Aldering, G., Wheeler, J. C., Höflich, P., Akerlof, C. W., & Rykoff, E. S. 2007, *ApJ*, 668, L99
 Quimby, R. M., et al. 2011, *Nature*, 474, 487
 Quimby, R. M., Kulkarni, S. R., Ofek, E., Kasliwal, M. M., Levitan, D., Gal-Yam, A., & Cenke, S. B. 2010, *The Astronomer’s Telegram*, 2492
 Rest, A., et al. 2005, *ApJ*, 634, 1103
 Schlegel, D. J., Finkbeiner, D. P., & Davis, M. 1998, *ApJ*, 500, 525
 Schmidt, G. D., Weymann, R. J., & Foltz, C. B. 1989, *PASP*, 101, 713
 Shklovskii, I. S. 1960, *Soviet Ast.*, 4, 243
 Smith, N., et al. 2007, *ApJ*, 666, 1116
 Smith, N., & McCray, R. 2007, *ApJ*, 671, L17
 Smith, N., & Owocki, S. P. 2006, *ApJ*, 645, L45
 Soderberg, A. M. 2007, PhD thesis, California Institute of Technology
 Soker, N., Frankowski, A., & Kashi, A. 2010, *New Astron.*, 15, 189
 Stubbs, C. W., Doherty, P., Cramer, C., Narayan, G., Brown, Y. J., Lykke, K. R., Woodward, J. T., & Tonry, J. L. 2010, *ApJS*, 191, 376
 Tonry, J., & Onaka, P. 2009, in *Advanced Maui Optical and Space Surveillance Technologies Conference*, ed. S. Ryan, The Maui Economic Development Board, E40
 Tremonti, C. A., et al. 2004, *ApJ*, 613, 898
 Valenti, S., et al. 2008, *MNRAS*, 383, 1485
 van der Horst, A. J., Rol, E., Wijers, R. A. M. J., Strom, R., Kaper, L., & Kouveliotou, C. 2005, *ApJ*, 634, 1166
 Weiler, K. W., Panagia, N., Montes, M. J., & Sramek, R. A. 2002, *ARA&A*, 40, 387
 Woosley, S. E. 2010, *ApJ*, 719, L204
 Woosley, S. E., Blinnikov, S., & Heger, A. 2007, *Nature*, 450, 390
 York, D. G., et al. 2000, *AJ*, 120, 1579
 Young, D. R., et al. 2010, *A&A*, 512, A70

TABLE 4
PS1 MDS + GALEX PHOTOMETRY FOR PS1-10KY

UT Date	MJD	Phase ^a (days)	NUV (mag)	g_{P1} (mag)	r_{P1} (mag)	i_{P1} (mag)	z_{P1} (mag)	y_{P1} (mag)
2010-Jun-26	55373.5	-12.0						21.21±0.18
2010-Jul-11	55388.6	-4.3					21.39±0.07	
2010-Jul-12	55389.5	-3.8		21.47±0.04	21.13±0.03			
2010-Jul-21	55398.6	0.8		21.41±0.12	21.10±0.08			
2010-Jul-23	55400.6	1.9					21.63±0.28	
2010-Jul-25	55402.4	2.8						21.30±0.25
2010-Jul-31	55408.5	5.9	>23.35			21.31±0.07		
2010-Aug-01	55409.5	6.4	>23.25				21.37±0.06	
2010-Aug-02	55410.5	7.0		22.08±0.13	21.30±0.06			
2010-Aug-03	55411.5	7.5				21.48±0.07		
2010-Aug-04	55412.5	7.9					21.25±0.07	
2010-Aug-05	55413.5	8.4		22.05±0.09	21.34±0.04			
2010-Aug-06	55414.5	9.0	>23.60			21.46±0.04		
2010-Aug-07	55415.6	9.5					21.43±0.10	
2010-Aug-08	55416.5	10.0	>23.58	22.40±0.11	21.43±0.04			
2010-Aug-09	55417.5	10.5				21.49±0.04		
2010-Aug-11	55419.0	11.3	>23.58					
2010-Aug-12	55420.5	12.0	>23.59					
2010-Aug-14	55422.5	13.1	>23.63	22.55±0.22	21.51±0.05			
2010-Aug-15	55423.5	13.6				21.63±0.04		
2010-Aug-16	55424.5	14.1	>23.66					
2010-Aug-17	55425.4	14.5		23.03±0.22	21.76±0.06			
2010-Aug-18	55426.5	15.1	>23.58			21.64±0.05		
2010-Aug-19	55427.5	15.6					21.66±0.08	
2010-Aug-20	55428.5	16.1	>23.54	23.33±0.24	22.10±0.08			
2010-Aug-22	55430.5	17.1	>23.56					21.63±0.24
2010-Aug-28	55436.4	20.2					21.98±0.14	
2010-Aug-29	55437.5	20.7		>22.68	22.05±0.17			
2010-Aug-30	55438.5	21.2				22.19±0.10		
2010-Aug-31	55439.3	21.7					21.77±0.09	
2010-Sep-02	55441.5	22.7				22.16±0.07		
2010-Sep-03	55442.5	23.3					21.90±0.11	
2010-Sep-04	55443.5	23.8	>23.57	>23.82	22.72±0.13			
2010-Sep-05	55444.4	24.3				22.43±0.10		
2010-Sep-06	55445.4	24.8	>23.63				22.07±0.13	
2010-Sep-07	55446.5	25.3		>23.34	22.74±0.27			
2010-Sep-08	55447.4	25.8				22.33±0.07		
2010-Sep-09	55448.4	26.3					22.17±0.13	
2010-Sep-10	55449.4	26.8		>23.62	22.92±0.15			
2010-Sep-11	55450.4	27.3				22.57±0.22		
2010-Sep-12	55451.5	27.9					22.39±0.26	
2010-Sep-13	55452.4	28.3		>23.53	23.03±0.21			
2010-Sep-14	55453.4	28.9				22.60±0.10		
2010-Sep-15	55454.4	29.4					22.37±0.17	
2010-Sep-16	55455.4	29.9		>23.43				
2010-Sep-17	55456.4	30.4				22.55±0.12		
2010-Sep-18	55457.3	30.9					22.53±0.21	
2010-Sep-19	55458.3	31.4		>22.02	>22.53			
2010-Sep-23	55463.4	33.5						>21.63
2010-Sep-24	55463.4	34.0						21.98±0.32
2010-Sep-25	55464.4	34.5						>21.76
2010-Sep-26	55465.5	35.0				23.01±0.26		
2010-Sep-27	55466.4	35.5					22.89±0.27	
2010-Sep-28	55467.3	36.0		>23.37	23.36±0.33			
2010-Sep-29	55468.3	36.5				23.22±0.20		
2010-Oct-04	55473.3	39.0		>23.36	>23.76			
2010-Oct-06	55475.2	40.0					22.61±0.23	
2010-Oct-09	55478.2	41.5					22.65±0.23	
2010-Oct-10	55479.2	42.0		>23.33	>23.62			
2010-Oct-11	55480.2	42.6				>23.43		
2010-Oct-12	55481.2	43.1					>22.90	
2010-Oct-13	55482.2	43.6		>23.49	>23.55			
2010-Oct-14	55483.2	44.1				23.57±0.25		
2010-Oct-15	55484.2	44.6					>23.01	
2010-Oct-17	55486.3	45.6				>23.11		
2010-Oct-23	55492.3	48.8						>21.74
2010-Oct-27	55496.3	50.8					>22.14	
2010-Oct-29	55498.2	51.8				>23.76		
2010-Oct-30	55499.2	52.3					>22.64	
2010-Oct-31	55500.2	52.8		>23.40	>23.65			
2010-Nov-01	55501.4	53.4				>23.50		
2010-Nov-02	55502.3	53.8					>22.95	
2010-Nov-03	55503.3	54.4		>23.59	>23.59			
2010-Nov-07	55507.3	56.4				>23.52		

TABLE 4 — *Continued*

UT Date	MJD	Phase ^a (days)	NUV (mag)	g_{P1} (mag)	r_{P1} (mag)	i_{P1} (mag)	z_{P1} (mag)	y_{P1} (mag)
2010-Nov-08	55508.2	56.9					>22.57	
2010-Nov-10	55510.3	57.9				>23.75		
2010-Nov-12	55512.3	59.0		>22.62				
2010-Nov-23	55523.3	64.6						>21.83
2010-Nov-30	55530.2	68.1			>22.73			
2010-Dec-05	55535.2	70.7					>22.90	
2010-Dec-06	55536.3	71.2		>22.94	>23.57			
2010-Dec-17	55547.2	76.8					>23.07	

^a In days relative to peak brightness, corrected for time dilation.

TABLE 5
PS1 MDS + GALEX PHOTOMETRY FOR PS1-10AWH

UT Date	MJD	Phase ^a (days)	NUV (mag)	g_{P1} (mag)	r_{P1} (mag)	i_{P1} (mag)	z_{P1} (mag)	y_{P1} (mag)
2010-Jun-26	55373.5	-77.9						>21.78
2010-Jul-11	55388.6	-69.0					>23.29	
2010-Jul-12	55389.5	-68.5		>23.61	>23.76			
2010-Jul-21	55398.6	-63.8			>22.62			
2010-Jul-23	55400.6	-62.7					>21.43	
2010-Jul-25	55402.4	-61.7						>21.31
2010-Jul-31	55408.5	-58.6				>22.94		
2010-Aug-01	55409.5	-58.0					>23.23	
2010-Aug-02	55410.5	-57.5		>23.10	>23.03			
2010-Aug-03	55411.5	-57.0				>23.39		
2010-Aug-04	55412.5	-56.5					>23.27	
2010-Aug-05	55413.5	-56.0		>23.47				
2010-Aug-06	55414.5	-55.4	>23.60			>23.70		
2010-Aug-07	55415.6	-54.8					>22.53	
2010-Aug-08	55416.5	-54.4	>23.58	>23.60	>23.70			
2010-Aug-11	55419.0	-53.3	>23.58					
2010-Aug-12	55420.5	-53.9	>23.60					
2010-Aug-14	55422.5	-51.1	>23.63	>23.52	>23.15			
2010-Aug-16	55424.5	-50.2	>23.66				>23.20	
2010-Aug-17	55425.4	-49.7		>23.48	>23.61			
2010-Aug-18	55426.5	-49.1	>23.69			>23.56		
2010-Aug-19	55427.5	-48.6					>23.35	
2010-Aug-20	55428.5	-48.1	>23.70	>23.43	>23.52			
2010-Aug-22	55430.5	-47.1						>21.85
2010-Aug-28	55436.4	-43.9					>23.04	
2010-Aug-29	55437.5	-43.4		>22.35	>22.65			
2010-Aug-30	55438.5	-42.8				>23.52		
2010-Aug-31	55439.3	-42.4					>23.38	
2010-Sep-01	55440.5	-41.8		>23.30	>23.33			
2010-Sep-02	55441.5	-41.3				>23.57		
2010-Sep-03	55442.5	-40.7					>22.97	
2010-Sep-04	55443.5	-40.2		>23.63	>23.61			
2010-Sep-05	55444.4	-39.8				>23.60		
2010-Sep-06	55445.4	-39.2					>23.27	
2010-Sep-07	55446.5	-38.6		>23.09	>22.95			
2010-Sep-08	55447.4	-38.2				>23.80		
2010-Sep-09	55448.4	-37.6					>23.33	
2010-Sep-10	55449.4	-37.1		>23.45	>23.66			
2010-Sep-11	55450.4	-36.6				>23.19		
2010-Sep-12	55451.5	-36.1					>22.83	
2010-Sep-13	55452.4	-35.6		>23.64	>23.59			
2010-Sep-14	55453.4	-35.0				>23.83		
2010-Sep-15	55454.4	-34.5					>23.29	
2010-Sep-16	55455.4	-34.0		>23.27	>23.56			
2010-Sep-17	55456.4	-33.5				>23.65		
2010-Sep-18	55457.3	-33.0					>23.11	
2010-Sep-19	55458.3	-32.5		>21.80	>22.10			
2010-Sep-23	55463.4	-30.3						>21.40
2010-Sep-24	55463.4	-29.8						>21.87
2010-Sep-26	55465.5	-28.7				>23.14		
2010-Sep-27	55466.4	-28.2					>23.18	
2010-Sep-28	55467.3	-27.7		>22.82	23.35±0.35			
2010-Sep-29	55468.3	-27.2				23.40±0.30		
2010-Oct-04	55473.3	-24.6		22.70±0.17	22.62±0.14			
2010-Oct-06	55475.2	-23.6					23.05±0.33	
2010-Oct-08	55477.2	-22.5				22.30±0.10		
2010-Oct-09	55478.2	-22.0					22.55±0.21	
2010-Oct-10	55479.2	-21.5		22.11±0.12	22.04±0.10			
2010-Oct-11	55480.2	-21.0				22.16±0.18		
2010-Oct-12	55481.2	-20.5					>22.60	
2010-Oct-13	55482.2	-19.9		21.89±0.11	21.77±0.07			
2010-Oct-14	55483.2	-19.4				21.94±0.06		
2010-Oct-15	55484.2	-18.9					21.98±0.14	
2010-Oct-17	55486.3	-17.8				21.70±0.14		
2010-Oct-27	55496.3	-12.6					21.58±0.23	
2010-Oct-29	55498.2	-11.6				21.58±0.06		
2010-Oct-30	55499.2	-11.0					21.66±0.12	
2010-Oct-31	55500.2	-10.5		21.63±0.07	21.43±0.05			
2010-Nov-01	55501.4	-9.9				21.57±0.09		
2010-Nov-02	55502.3	-9.4					21.54±0.11	
2010-Nov-03	55503.3	-8.9		21.54±0.10	21.40±0.07			
2010-Nov-07	55507.3	-6.8				21.32±0.05		
2010-Nov-08	55508.2	-6.3					21.48±0.10	
2010-Nov-10	55510.3	-5.3				21.21±0.04		

TABLE 5 — *Continued*

UT Date	MJD	Phase ^a (days)	NUV (mag)	g_{P1} (mag)	r_{P1} (mag)	i_{P1} (mag)	z_{P1} (mag)	y_{P1} (mag)
2010-Nov-12	55512.3	−4.2		21.54±0.23				
2010-Nov-23	55523.3	1.6						>21.61
2010-Dec-04	55534.3	7.3				21.28±0.08		
2010-Dec-05	55535.2	7.8					21.23±0.08	
2010-Dec-06	55536.3	8.4		>22.21				
2010-Dec-17	55547.2	14.2					21.64±0.10	

^a In days relative to peak brightness, corrected for time dilation.